

Prediction of Room-Temperature Electric Field Reversal of Magnetization in the Family of $A_4B_3O_9$ Layered Oxides

Urmimala Dey,¹ Emma E. McCabe,¹ and Nicholas C. Bristowe^{1,*}

¹Centre for Materials Physics, Durham University,
South Road, Durham DH1 3LE, United Kingdom

(Dated: May 3, 2024)

The promise of a strong magnetoelectric (ME) coupling in a multiferroic (MF) material is not only of fundamental interest, but also forms the basis of next generation memory devices where the direction of magnetization can be reversed by an external electric field. Using group-theory led first-principles calculations, we determine the ME properties of a relatively understudied family of layered oxides with the general formula $A_4B_3O_9$. We show how the tetrahedral rotations in these oxides can lead to a variety of hitherto unknown structural phases with different symmetries. In particular, a polar phase in the $Cmc2_1$ space group has been identified where a weak ferromagnetic mode arises spontaneously via a canting of the antiferromagnetically ordered B -site spins. In this polar phase, the polar mode couples to the magnetic modes through a rare Γ -point ME-MF coupling scheme such that the net magnetization can be directly reversed by an electric field switching of the polar mode. Moreover, in agreement with previous experimental observations, we predict room-temperature magnetism in $A_4B_3O_9$ layered oxides which is supported by our calculations of the magnetic exchange interaction parameters, further indicating the potential of these compounds in practical technological applications.

INTRODUCTION

Magnetoelectric multiferroic (ME-MF) materials with intrinsic cross-coupling between electrical and magnetic order parameters are promising for the next generation memory devices where an external electric field can switch the direction of magnetization leading to enhanced speed and reduced power consumption [1–6]. So far, despite intensive research efforts, only a handful of bulk materials with electric field switchable magnetism have been predicted and observed in experiments [6–11], and unfortunately none that order at room-temperature (RT). Therefore, the search for ME-MF materials with RT electric field control of magnetization remains of utmost importance for realistic applications in memory devices [6, 12].

Such control of magnetization can be achieved in a (single phase) antiferromagnetic (AFM) ME-MF material where weak ferromagnetism (wFM) arises due to canting of the collinear AFM spins via the Dzyaloshinskii-Moriya interaction (DMI) [14–16]. Depending on the crystal structure and underlying symmetries, electric polarization (\mathbf{P}) can couple to the net magnetization (\mathbf{M}) in these materials via different mechanisms [7, 8, 17]. The advantage of these type of strategies is that, since the couplings are at odd-order (sometimes called ‘improper’ couplings), switching polarization (\mathbf{P}) can necessarily switch magnetization (\mathbf{M}). Inspired by these ME schemes, Senn and Bristowe have enumerated the possible ME-MF couplings in perovskites using a group-theoretical approach [13]. However, since AFM orderings in perovskite systems are always described by zone-

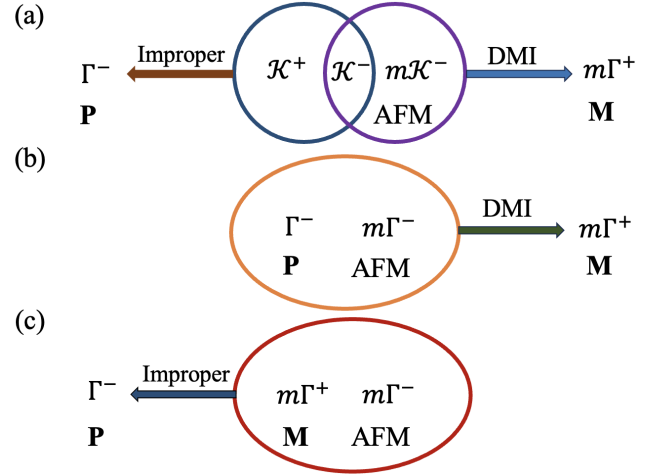


FIG. 1. Trilinear coupling terms in the free energy expansion representing (a) \mathcal{K} -point ME-MF scheme in perovskites involving \mathbf{P} and \mathbf{M} [13], where \mathcal{K} denotes a general zone-boundary point. $m\mathcal{K}^-$ is the irrep associated with AFM ordering, whereas \mathcal{K}^- and \mathcal{K}^+ are the irreps representing nonpolar and nonmagnetic order parameters. (b) Γ -point coupling scheme allowing for the reversal of \mathbf{M} with \mathbf{P} in systems with larger unit cells where AFM order parameters transform as $m\Gamma^-$ irreps. (c) The same Γ -point ME-MF scheme in type-II MFs where the AFM mode couples with \mathbf{M} to induce improper ferroelectricity.

boundary irreducible representations (irreps) of the parent space group, even the lowest-order ME-MF coupling schemes must involve a two-step process, each step contributing odd order energy terms in \mathbf{P} and \mathbf{M} separately with dependent order parameters [13], as shown in Fig. 1(a).

More generally, however, it should be possible to con-

* nicholas.bristowe@durham.ac.uk

construct a simpler Γ -point scheme where \mathbf{P} and \mathbf{M} couple with a Γ -point AFM ordering mode in an ‘improper’ manner such that the crystal momenta, inversion symmetry and the time reversal symmetry are preserved (see Figs. 1(b)–(c)). When \mathbf{P} and AFM ordering modes couple to give rise to a net \mathbf{M} induced by the DMI, application of an electric field can directly reverse \mathbf{M} via the reversal of \mathbf{P} as the primary AFM order parameter is less likely to switch. This simpler Γ -point ME-MF scheme, shown in Fig. 1(b), allows for the switching mechanism to be contained in only one trilinear term but likely requires proper ferroelectricity and has rarely been observed [7, 18] to the best of our knowledge. On the other hand, the same Γ -point coupling in Fig. 1(c) can also explain the induction of improper ferroelectricity observed in some type-II MFs [19, 20] where the AFM mode couples with \mathbf{M} to break the spatial inversion symmetry of the system, though this usually requires complex magnetic structures.

Using first-principles calculations guided by group-theoretical analysis, we identify a hitherto unknown polar phase of bulk $A_4B_3O_9$ layered oxides (A : rare-earth and/or alkali-earth cations; B : Co, Ni, Fe) where an applied electric field can switch the magnetization between 180° symmetry equivalent states through the Γ -point ME-MF scheme shown in Fig. 1(b). Our phonon calculations reveal that the high-symmetry paraelectric phase of these layered oxides is unstable against a zone-center polar distortion. A wFM mode arises spontaneously in the resulting polar phase via a canting of the ground state AFM spin ordering of the magnetic B -site cations. The polar mode couples to the wFM mode and the AFM order via the Γ -point scheme described above, giving rise to a non-linear ME effect where magnetization can be reversed by an electric field via the reversal of the polar mode. Previous experimental studies on these layered oxides demonstrated long-range AFM ordering of the spins above RT [21, 22], indicating the possibility of RT electric field switching of magnetization in $A_4B_3O_9$ layered oxides, which is further supported by our calculations of magnetic exchange interaction parameters. We explain the design principles to stabilize the polar phase with non-trivial ME effect starting from an otherwise nonpolar structure without net magnetization, in the hope of inspiring future experimental work.

RESULTS

Parent $A_4B_3O_9$ structure and its instabilities

Fig. 2 shows the crystal structure of the $A_4B_3O_9$ layered oxides which contains slabs of (oxygen-deficient) perovskite-type ABO_3 triple layers translated relative to each other in the basal plane, and separated by rocksalt-type AO layers. A -sites are occupied by rare-earth and/or alkali-earth elements while the B -sites are occupied by transition metal ions. Oxygen vacancies are

formed at the central perovskite layer in each block in an ordered manner giving rise to planes of BO_6 octahedra and BO_4 tetrahedra alternating along the out-of-plane direction. The $A_4B_3O_9$ layered oxides can, therefore, be described as $n = 3$ Ruddlesden-Popper phases with oxide vacancies at the equatorial sites in the central layers of the perovskite blocks which give rise to layers of BO_4 tetrahedra reminiscent of those in the brownmillerite (BM) phases [22–25].

$A_4B_3O_9$ layered oxides appear relatively understudied in literature compared to other oxygen-deficient layered compounds like BMs [26–29] and Grenier phases [30–33]. The parent phase of these layered oxides has $Cmcm$ symmetry (no. 63), which contains no rotations of the tetrahedra but allows for tilting of the BO_6 octahedra, as shown in Fig. 2(a). The parent $Cmcm$ structure can also be described as a disordered phase with no long-range ordering of the tetrahedra. Previous experiments on $LnSr_3Fe_3O_9$ (Ln : La, Pr, Nd) show that these layered oxides crystallize into an average structure of $Cmcm$ symmetry without any signature of long-range ordering of the tetrahedral chains [25, 34–36]. However, the tetrahedra in these layered compounds can exhibit long range ordering by rotating about the out-of-plane axis in clockwise and anti-clockwise directions leading to the formation of left-handed and right-handed apex-linked 1D tetrahedral chains with distinct chiralities, analogous to the BMs. Since the tetrahedra are corner-connected, rotation about the out-of-plane direction is cooperative i.e. rotation of one tetrahedron (e.g., clockwise) about the out-of-plane direction causes the nearest corner-connected in-plane tetrahedra to rotate in the opposite direction (e.g., anti-clockwise).

Depending on the relative ordering of the tetrahedral chains within the unit cell, it is possible to observe a number of structurally diverse phases. When all the tetrahedra rotate in the same direction (either left-handed or right-handed), the dipole moments arising from the displacement of cations away from the center of each tetrahedron add up, resulting in a polar structure in the $Cmc2_1$ space group (no. 36) which is associated with a polar mode transforming as the $\Gamma_2^-(a)$ irrep of the parent $Cmcm$ phase (see Fig. 2(b)). Note that in the $Cmc2_1$ structure, electric polarization is in-plane and along the tetrahedral chain direction, analogous to the $Ima2$ phase of BMs [28]. On the other hand, if the tetrahedra rotate in opposite senses in successive layers (i.e. intralayer polarization switching/reversing from layer to layer), the dipole moments from each layer cancel out forming an antipolar structure as depicted in Fig. 2(b). This antipolar structure is related to the $Cmcm$ phase by the $Y_2^-(a)$ irrep which reduces the symmetry from $Cmcm$ to $Pm\bar{c}n$ (no. 62, bca setting). Again, this model is analogous to the $Pnma$ model observed in BMs [28]. A neutron diffraction study by Hansteen et al. on $La_4Co_3O_9$ reveals the formation of long range ordering of the CoO_4 tetrahedra along the out-of-plane direction leading to an antipolar phase in the $Pnma$ space group (no. 62) [22].

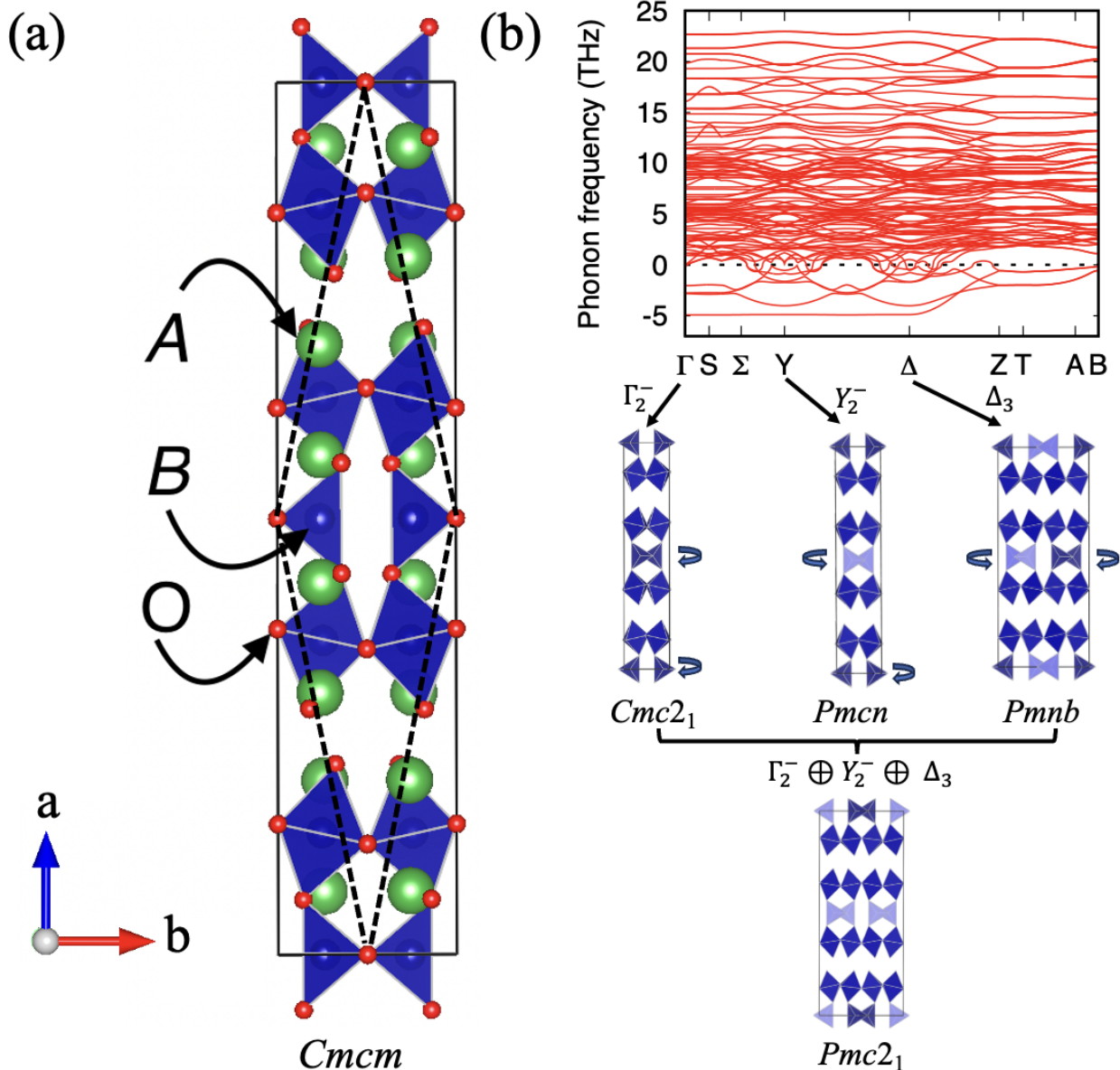


FIG. 2. (a) Crystal structure of the high-symmetry $Cmcm$ phase of the $A_4B_3O_9$ layered oxides consisting of planes of BO_6 octahedra and BO_4 tetrahedra alternating along the out-of-plane direction. Conventional and primitive unit cells are shown by solid and dashed lines, respectively. (b) Phonon spectrum for the $Cmcm$ structure of $Nd_4Co_3O_9$ (as a representative of $A_4B_3O_9$ layered oxides) along the $\Gamma(0, 0, 0) - S(0, 0.5, 0) - \Sigma(0.25, 0.25, 0) - Y(0.5, 0.5, 0) - \Delta(0.75, 0.25, 0) - Z(0, 0, 0.5) - T(0.5, 0.5, 0.5) - A(0.25, 0.25, 0.5) - B(0.75, 0.25, 0.5)$ direction of the BZ (in the primitive basis). The phonon dispersion calculated with the ground state G-AFM spin ordering shows a number of instabilities at the zone center and zone boundary points, which when condensed, result in a variety of structural variants arising from the cooperative rotations of the tetrahedral units.

It is interesting to note that different intralayer and interlayer tetrahedral twisting patterns can further lead to a variety of other distinct phases resulting in superstructures with longer periods, as observed in a local scale in $Ca_4Fe_2Mn_{0.5}Ti_{0.5}O_9$ [37] (see Fig. S4 of the Supplementary Information (SI)). An example of a superstructure with intralayer switching of tetrahedral rotation patterns described by $Pmnb$ symmetry (no. 62) is shown in Fig. 2(b), which is associated with the $\Delta_3(a, -a)$ irrep of

the parent phase and similar to the $Pbcm$ phase of the BMs [28]. We have identified another novel polar phase with $Pmc2_1$ symmetry which contributes an energy term of the form $Q_{\Delta_3}^2 Q_{\Gamma_2^-} Q_{Y_2^-}$ in the free energy expansion of the high symmetry phase. This kind of novel ferroelectric phase with a quadratic-bilinear coupling has also been observed in BM oxides [38].

Indeed, our phonon calculations for the paraelectric $Cmcm$ structure of $Ln_4B_3O_9$ (Ln : La, Pr, Nd; B :

Co, Ni) and $\text{La}A'\text{Fe}_3\text{O}_9$ (A' : Sr, Ca) compounds reveal a number of instabilities at the zone center and zone boundary points, which when condensed, result in a variety of structural variants arising from the cooperative rotations of the tetrahedral units, as shown in Fig. 2(b). The phonon spectra calculated for the $Cmcm$ phase of all the considered $A_4B_3O_9$ systems show qualitatively similar features with a strongly unstable flat phonon branch along the Γ -S- Σ -Y- Δ direction in the Brillouin zone (BZ) related to the tetrahedral chain ordering distortions. The presence of a flat phonon band indicates the energetic easiness to transform between different tetrahedral rotation patterns (at the harmonic level, at least). Moreover, the unstable phonons can condense in at any point between Γ -S- Σ -Y- Δ to lower the overall energy of the system and may lead to a series of closely-related superstructures with increasingly complex tilt patterns as described in detail in the SI.

Tuning between Polar and Antipolar ground states

Starting with the optimized structures, we compute the energy gain on going from the nonpolar $Cmcm$ phase to the polar $Cmc2_1$ phase (ΔE_{NP}) across the three sets of compounds containing different B -site cations ($B = \text{Co, Ni and Fe}$). As seen from Table I, all the materials are insulating with a bandgap in the range of 1.2 eV to 2.4 eV (see Figs. S1 and S7). In each series, inclusion of smaller A -site cations is found to increase the degree of tetrahedral rotations leading to higher stability of the low-symmetry phases as shown in Table I.

TABLE I. Energetics and bandgaps of the considered $A_4B_3O_9$ layered oxides. Here, ΔE_{NP} is the energy gain on going from the nonpolar $Cmcm$ phase to the polar $Cmc2_1$ phase. ΔE_{PA} and $Q_{\Gamma_2^-}$ denote relative energy of the polar $Cmc2_1$ phase with respect to the antipolar $Pm\bar{c}n$ phase and the amplitude of the polar mode, respectively. Bandgaps are determined for the lowest energy phases, while $Q_{\Gamma_2^-}$ is calculated for the relaxed $Cmc2_1$ structure of each compound. G-AFM spin ordering is considered for all the calculations. For $\text{La}A'_3\text{Fe}_3\text{O}_9$ ($A' = \text{Ca, Sr}$) layered oxides, results are given only for the electron doped models (see SI for details).

B -site element	Layered oxide	ΔE_{NP} (eV/f.u.)	ΔE_{PA} (meV/f.u.)	$Q_{\Gamma_2^-}$ (\AA)	Bandgap (eV)
Co	$\text{La}_4\text{Co}_3\text{O}_9$	0.63	0.42	1.67	2.0
	$\text{Pr}_4\text{Co}_3\text{O}_9$	1.09	0.11	1.72	1.9
	$\text{Nd}_4\text{Co}_3\text{O}_9$	1.27	-3.21	2.22	2.4
Ni	$\text{La}_4\text{Ni}_3\text{O}_9$	0.55	-0.15	1.60	1.3
	$\text{Pr}_4\text{Ni}_3\text{O}_9$	0.73	-0.32	1.65	1.2
	$\text{Nd}_4\text{Ni}_3\text{O}_9$	0.76	-0.71	1.68	1.2
Fe	$\text{LaSr}_3\text{Fe}_3\text{O}_9$	0.44	0.003	1.70	1.9
	$\text{LaCa}_3\text{Fe}_3\text{O}_9$	0.74	-9.10	1.75	1.7

In Table I, we tabulate the energy of the polar $Cmc2_1$ phase relative to the antipolar $Pm\bar{c}n$ phase (ΔE_{PA}) for all the considered layered compounds. The antipolar phase is the ground state for $\text{La}_4\text{Co}_3\text{O}_9$ in agreement with earlier experimental results [22]. However, as we decrease the A -cation size from La^{3+} to Nd^{3+} , the antipolar phase becomes metastable and the ground state acquires finite polarization with $Cmc2_1$ symmetry. A similar trend in ΔE_{PA} is observed in the Ni- and Fe-series. Furthermore, the amplitude of the polar mode ($Q_{\Gamma_2^-}$) computed for the fully relaxed $Cmc2_1$ structure of each compound shows that inclusion of smaller A -site cations increases the polar distortion. Note that this trend in ΔE_{PA} is opposite in BMs where larger tetrahedral chain rotations favor the antipolar phase [39]. In the case of $\text{LaSr}_3\text{Fe}_3\text{O}_9$, ΔE_{NP} is smaller and the polar and antipolar phases have almost identical energies ($\Delta E_{\text{PA}} \sim 0.003$ meV/f.u.), implying that there might not be any long range ordering of the tetrahedral chains, consistent with the experimental observation of an average $Cmcm$ structure [34, 35]. However, these results in Table I are given only for the electron doped models of $\text{La}A'_3\text{Fe}_3\text{O}_9$ ($A' = \text{Ca, Sr}$) and as shown in Table S8, relative energies of the polar and antipolar phases of $\text{La}A'_3\text{Fe}_3\text{O}_9$ vary depending on the cation ordering model considered.

We next check the stability of the polar $Cmc2_1$ structure of the compounds with negative ΔE_{PA} against the formation of superstructures with longer periods of tetrahedral twisting patterns (see SI for details). Focusing on the Co-series (due to the challenges of modeling A -cation disorder with DFT in the Fe-series, and with the Ni-series not yet synthesized), we find that polar $Cmc2_1$ phase is the ground state of $\text{Nd}_4\text{Co}_3\text{O}_9$. Dynamical stability of the $Cmc2_1$ structure of $\text{Nd}_4\text{Co}_3\text{O}_9$ is shown in Fig. S3(c).

Electric field switching of Magnetization

$A_4B_3O_9$ compounds are shown to possess above RT magnetism in earlier experiments [21, 22, 25, 34]. Previous neutron diffraction studies on $\text{LnSr}_3\text{Fe}_3\text{O}_9$ (Ln : La, Pr, Nd) [25, 34] and $\text{La}_4\text{Co}_3\text{O}_9$ [22] have also characterized the ground state magnetic structures of these materials where the spins are found to order antiferromagnetically above RT along the tetrahedral chain direction. Considering four collinear spin configurations of the B -site cations in the lowest energy phases given in Table I, namely, A-type antiferromagnetic (A-AFM), C-type antiferromagnetic (C-AFM), G-type antiferromagnetic (G-AFM), and ferromagnetic (FM) spin arrangements, we first confirm the G-AFM magnetic structure, shown in Fig. 3(a), as the ground state for the Co-series compounds as observed in earlier experiments [22]. Non-collinear magnetic calculations including SOC further reveal that all the systems have magnetic easy axis along the tetrahedral chain direction i.e. in the plane along the [001] direction in agreement with previous experi-

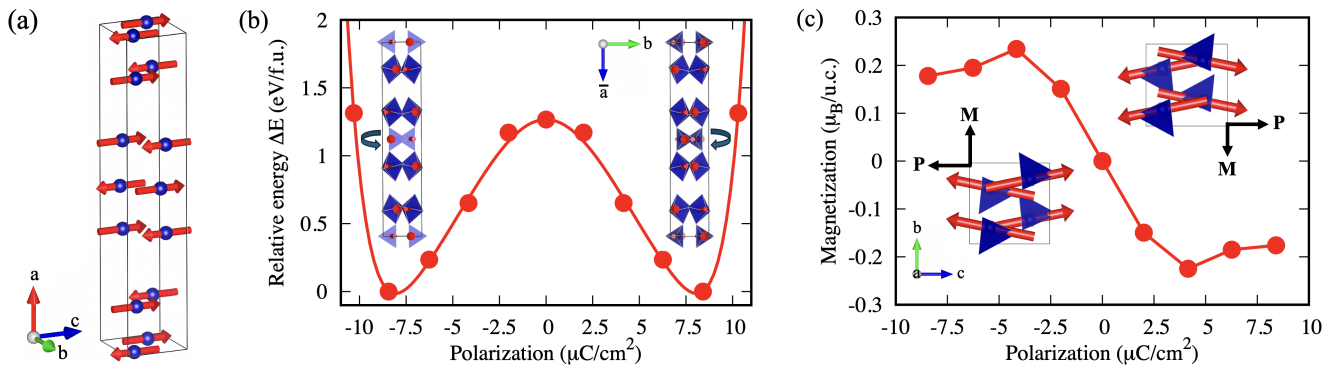


FIG. 3. (a) Ground state G-AFM magnetic configuration of Nd₄Co₃O₉ showing the spin magnetic moments on the Co²⁺ sites, denoted by red arrows, along the tetrahedral chain direction. (b) Polarization switching path in Nd₄Co₃O₉ calculated for the polar *Cmc*2₁ phase with G-AFM magnetic configuration. Sense of rotations of the tetrahedra is flipped as we go from the +**P** states to the -**P** states as seen from the corresponding crystal structures. (c) Calculated net magnetization as a function of the polar mode amplitude demonstrating the reversal of magnetization with the reversal of the electric polarization. Spin moments in the +**P** and -**P** states have opposite canting directions resulting in opposite net magnetization -**M** and +**M** in the +**P** and -**P** states, respectively, showing the possibility of observing electric field switching of magnetization in Nd₄Co₃O₉ layered oxide. Note that only the magnetic moments on the tetrahedral sites are shown for clarity.

mental observations [22, 34]. It is important to note that the orthorhombic distortions in the *A*₄*B*₃O₉ structures are large enough to experimentally distinguish between the moments being along the tetrahedral chain direction vs. perpendicular to the chain direction, unlike in some other layered perovskite-related systems [40–42]. Moreover, the spins are along the tilt axis of the *BO*₆ octahedra, consistent with the in-plane anisotropy observed for La₂CoO₄ [40, 41]. Details of the ground state crystal structures and magnetic configurations are given in the SI.

Interestingly, we find that in the *Cmc*2₁ phase, the polar mode induces a net magnetization perpendicular to the tetrahedral chain direction (i.e. along [010]) via a canting of the antiferromagnetically ordered (G- and C-AFM) collinear spins of the *B*-site cations along the chain direction (i.e. along [001]), which is otherwise absent in the paraelectric *Cmcm* phase. Both G- and C-AFM spin configurations in the *Cmc*2₁ structure correspond to the magnetic space group *Cm'*c2'₁ (magnetic point group *m'**m*2') which is related to the high symmetry *Cmcm* space group by a polar distortion transforming as the $\Gamma_2^-(a)$ irrep and two magnetic distortions transforming as $m\Gamma_3^-(a)$ and $m\Gamma_4^+(a)$ irreps. The $m\Gamma_3^-$ irrep is associated with the primary AFM magnetic ordering, whereas the $m\Gamma_4^+$ irrep represents the secondary wFM mode. Group theoretical analysis reveals that these three modes couple in an ‘improper’ manner, contributing a trilinear energy term of the form:

$$\mathcal{F} = \gamma Q_{\Gamma_2^-} Q_{m\Gamma_4^+} Q_{m\Gamma_3^-}$$

in the free energy expansion of the parent phase where, γ is the expansion coefficient.

As a consequence of this Γ -point coupling, reversal of **P** via an electric-field would necessarily require reversal

of just one of the two magnetic modes, with the wFM canting being the more likely candidate. Hence we expect 180° reversal of **M** with an applied electric field.

Fig. 3(b) shows the polarization double well in Nd₄Co₃O₉ calculated for the ground state G-AFM magnetic configuration in the polar *Cmc*2₁ phase with polarization along [001]. Here, we plot the relative energy of the *Cmc*2₁ structure (ΔE) as a function of the polar mode amplitude ($Q_{\Gamma_2^-}$). As seen, ΔE is maximum for the *Cmcm* phase which corresponds to $P = M = 0$. As we increase $Q_{\Gamma_2^-}$, ΔE decreases on both sides reaching a minimum at the relaxed value of $Q_{\Gamma_2^-}$ and corresponds to $P^0 \sim \pm 8.41 \mu\text{C}/\text{cm}^2$ which is about 2–4 times larger than the electric polarization in BMs [28, 29, 38]. Fig. 3(c) shows the resulting net magnetization for the different amplitudes of the polar mode. For small P , the magnetization varies linearly with $Q_{\Gamma_2^-}$ which is consistent with the Γ -point scheme shown in Fig. 1(b) and reaches a value of $M^0 \sim \pm 0.18 \mu_B$ per unit cell along [010] for the relaxed value of $Q_{\Gamma_2^-}$. Interestingly, the spin canting angles are flipped as we reverse the electric polarization resulting in opposite net magnetization -**M** and +**M** in the +**P** and -**P** states, respectively, demonstrating the switching of magnetization via the reversal of the polar mode. Our first-principles calculations thus predict Nd₄Co₃O₉ as an ideal candidate for observing the electric field switching of magnetization.

Finally, to investigate the possibility of RT magnetization switching in Nd₄Co₃O₉, we calculate the magnetic exchange parameters (*J*'s) of Nd₄Co₃O₉ and compare them with the *J*'s of La₄Co₃O₉ where RT long range magnetic order has been experimentally observed [21, 22]. We find that the calculated *J*'s for the *Pmcn* structure of La₄Co₃O₉ are almost identical to those computed for

the ground state $Cmc2_1$ structure of $Nd_4Co_3O_9$, indicating that $Nd_4Co_3O_9$ is also likely to exhibit long range magnetic ordering at RT. Computational details of the magnetic exchange interaction parameters are given in the SI.

DISCUSSION

We have proposed a Γ -point ME-MF scheme that might exist in systems with larger unit cells where the AFM mode transforms as $m\Gamma^-$ irrep. This allows for the reversal of DMI-induced magnetization with an external electric field and has rarely been observed [7, 18] to the best of our knowledge.

By performing systematic first-principles calculations on $A_4B_3O_9$ layered oxides (A : rare-earth and/or alkali-earth cations; B : Co, Ni, Fe), we find a variety of previously unknown structurally distinct phases with different space group symmetries arising from the cooperative rotations of the tetrahedral units. In particular, a polar structure with $Cmc2_1$ symmetry has been identified where wFM is induced spontaneously via a canting of the ground state AFM ordered (G- and C-AFM) spins of the B -site cations. The wFM mode, transforming as the $m\Gamma_4^+$ irrep, combines with the polar mode Γ_2^- and the AFM mode $m\Gamma_3^-$ in an ‘improper’ fashion so that reversal of the wFM mode by an electric field proceeds via the reversal of the polar mode as the primary AFM mode is less likely to switch.

Our calculations also suggest that smaller A -site cations can induce a larger polar distortion, stabilizing the polar $Cmc2_1$ structure with net magnetization. Inclusion of smaller A -site cations is also found to increase the degree of tetrahedral rotations leading to higher stability of the low-symmetry phases. The calculated values of ΔE_{NP} which generally gives an estimate of the switching barrier are in the range of 0.44 eV to 1.27 eV per formula unit and of the same order of magnitude calculated for similar geometric ferroelectrics [29, 43, 44]. ΔE_{NP} measures the upper bound of the energy necessary to completely switch the electric polarization in the $Cmc2_1$ phase which requires simultaneous reversal of the directions of all the tetrahedral units. However, in reality polarization reversal depends on domain wall motion, and furthermore, could involve several different intermediate structural phases obtained by switching the tetrahedra one by one. As a result, the actual energy barrier necessary to switch between $+\mathbf{P}$ and $-\mathbf{P}$ states are usually much lower than the magnitude of ΔE_{NP} , as observed in related BM oxides [29]. Previous experimental evidence of ferroelectric switching in thin films of BMs with similar magnitudes of ΔE_{NP} [44] suggests the possibility of experimental observation of electric field reversal of polarization in $A_4B_3O_9$ layered oxides. However, one should note that while these layered oxides draw similarities with BMs, the BMs have not been found to allow for a 180° ME-MF switching scheme.

From our first-principles calculations, we put forward $Nd_4Co_3O_9$ with G-AFM ordered $Cmc2_1$ ground state as an ideal candidate to observe the ME-MF switching. Moreover, in analogy with the experimental observation of RT magnetism in $La_4Co_3O_9$, we predict the RT electric field control of magnetization in $Nd_4Co_3O_9$, which is further supported by the calculations of magnetic exchange interaction parameters and thus indicates the possibility of RT applications of $Nd_4Co_3O_9$ in the next generation memory devices. It is important to note that because of the similar ionic radii of La^{3+} (1.36 Å, C.N. 12) and Nd^{3+} (1.27 Å, C.N. 12), the Nd-analog of $LaSr_3Fe_3O_9$ has been successfully synthesized in previous experiments [25]. Therefore, it is likely that the Nd-substituted analog of $La_4Co_3O_9$ can also be synthesized. Moreover, Olafsen et al. have demonstrated the preparation of the oxidized compound $Nd_4Co_3O_{10}$ [45], showing the possibility of synthesizing its reduced derivative.

As discussed in the SI, another competing magnetic structure (G*-AFM) has been identified which does not allow for a wFM mode in the $Cmc2_1$ phase by symmetry, but is very close in energy to the G-AFM magnetic structure of $A_4B_3O_9$ oxides. Note that G*-AFM spin configuration has been reported to be the ground state for the Fe-series compounds [34]. The small energy difference between the G- and G*-AFM spin orderings might lead to stacking faults in the magnetic structures of the Co-series layered oxides [40, 46]. However, if G- vs. G*-AFM ordering in $Nd_4Co_3O_9$ becomes an issue experimentally (i.e., there are domains of each), one could try to stabilize the G-AFM magnetic ordering by cooling through the phase transition with electric and magnetic fields. Furthermore, substitutional doping at the transition metal site might also allow the interlayer interactions to be tuned, stabilizing one magnetic structure over the other [47].

In summary, we have identified a series of new layered oxides which have all the necessary ingredients for the elusive control of magnetization with an electric field at RT. Apart from important memory applications, these materials show a range of intriguingly subtle magnetic and structural phases, apparently coupled to their layered and vacancy ordered nature. This understanding will likely provide new opportunities within related active fields on Ruddlesden-Popper and BM materials such as memristors [48, 49], catalysis [50, 51], photoferroics [52, 53], and 2D magnetism [54, 55].

METHODS

First-principles calculations were performed within the density functional theory (DFT) framework using the projected augmented wave (PAW) method implemented in the VASP code [56], version 6.3.2. In order to accurately describe the equilibrium structures of the bulk $A_4B_3O_9$ oxides, PBEsol version of generalised gradient approximation (GGA) was chosen as the exchange-

correlation functional [57]. PAW pseudopotentials (PBE, version 5.4) [58] were used for all the calculations with the following valence configurations: $5s^25p^65d^16s^2$ (La), $5s^25p^65d^16s^2$ (Pr), $5s^25p^65d^16s^2$ (Nd), $4s^24p^25s^2$ (Sr), $3s^23p^24s^2$ (Ca), $3p^63d^74s^2$ (Co), $3p^63d^84s^2$ (Ni), $3p^63d^64s^2$ (Fe), and $2s^22p^4$ (O). Correlation effects were considered within the GGA+ U formalism introduced by Dudarev et al. [59] using an effective on-site Hubbard parameter $U_{\text{eff}} = 5.0$ eV, 5.15 eV and 4.0 eV for the $3d$ states of Co^{2+} , Ni^{2+} and Fe^{3+} ions, respectively [60–63]. The U_{eff} values were varied within a reasonable range to check the stability of the ground states. Effect of Hund’s parameter J on wFM moments was tested within the framework of Liechtenstein [64] as implemented in VASP. Convergence tests were performed on a 64-atom $Cmcm$ unit cell of $\text{La}_4\text{Co}_3\text{O}_9$ which showed that a plane wave cutoff of 800 eV and k -mesh grid of $1 \times 5 \times 6$ in the full BZ were sufficient to reach converged results. Full relaxations were performed until the Feynman-Hellman forces on each atom were less than 1 meV/Å with an energy convergence criterion set at 10^{-9} eV. Spin-orbit coupling (SOC) effects were included self-consistently in the non-collinear calculations. We used the finite displacement method implemented in PHONOPY [65] to calculate the phonon dispersions using a $1 \times 2 \times 2$ phonon supercell. Phonon spectra were computed for the primitive cell using the transformation matrix $[-0.5 \ 0.0 \ 0.0, 0.5 \ -0.5 \ 0.0, 0.0 \ 0.0 \ 1.0]$. We employed the Berry phase method [66, 67] within VASP to compute the spontaneous electric polarization. The web-based ISOTROPY software suit [68] was used for symmetry mode analyses, and visualisation of crystal structures and magnetic configurations were done by VESTA [69].

REFERENCES

- [1] Lottermoser, T. *et al.* Magnetic phase control by an electric field. *Nature* **430**, 541–544 (2004).
- [2] Ederer, C. & Spaldin, N. A. Electric-field-switchable magnets: The case of bnif_4 . *Phys. Rev. B* **74**, 020401 (2006).
- [3] Zhao, T. *et al.* Electrical control of antiferromagnetic domains in multiferroic bifeo_3 films at room temperature. *Nat. Mater.* **5**, 823–829 (2006).
- [4] Fiebig, M., Lottermoser, T., Meier, D. & Trassin, M. The evolution of multiferroics. *Nat. Rev. Mater.* **1**, 1–14 (2016).
- [5] Spaldin, N. A. & Ramesh, R. Advances in magnetoelectric multiferroics. *Nat. Mater.* **18**, 203–212 (2019).
- [6] Fert, A., Ramesh, R., Garcia, V., Casanova, F. & Bibes, M. Electrical control of magnetism by electric field and current-induced torques. *Rev. Mod. Phys.* **96**, 015005 (2024).
- [7] Fennie, C. J. Ferroelectrically induced weak ferromagnetism by design. *Phys. Rev. Lett.* **100**, 167203 (2008).
- [8] Benedek, N. A. & Fennie, C. J. Hybrid improper ferroelectricity: A mechanism for controllable polarization-magnetization coupling. *Phys. Rev. Lett.* **106**, 107204 (2011).
- [9] Tokunaga, Y., Taguchi, Y., Arima, T.-h. & Tokura, Y. Electric-field-induced generation and reversal of ferromagnetic moment in ferrites. *Nat. Phys.* **8**, 838–844 (2012).
- [10] Chai, Y. S. *et al.* Electrical control of large magnetization reversal in a helimagnet. *Nat. Commun.* **5**, 4208 (2014).
- [11] Kocsis, V. *et al.* Magnetization-polarization cross-control near room temperature in hexaferrite single crystals. *Nat. Commun.* **10**, 1247 (2019).
- [12] Ramesh, R. & Manipatruni, S. Electric field control of magnetism. *Proc. R. Soc. A* **477**, 20200942 (2021).
- [13] Senn, M. S. & Bristowe, N. C. A group-theoretical approach to enumerating magnetoelectric and multiferroic couplings in perovskites. *Acta Crystallogr. A: Found. Adv.* **74**, 308–321 (2018).
- [14] Dzyaloshinsky, I. A thermodynamic theory of “weak” ferromagnetism of antiferromagnetics. *J. Phys. Chem. Solids* **4**, 241–255 (1958).
- [15] Moriya, T. New mechanism of anisotropic superexchange interaction. *Phys. Rev. Lett.* **4**, 228–230 (1960).
- [16] Scott, J. & Blinc, R. Multiferroic magnetoelectric fluorides: why are there so many magnetic ferroelectrics? *J. Phys. Condens. Matter* **23**, 113202 (2011).
- [17] Yang, Y., Ñíguez, J., Mao, A.-J. & Bellaiche, L. Prediction of a novel magnetoelectric switching mechanism in multiferroics. *Phys. Rev. Lett.* **112**, 057202 (2014).
- [18] Ederer, C. & Fennie, C. J. Electric-field switchable magnetization via the dzyaloshinskii-moriya interaction: Fetio_3 versus bifeo_3 . *J. Phys. Condens. Matter* **20**, 434219 (2008).
- [19] Clarke, G. R., Lees, M. R., Ritter, C., da Silva, I. & Senn, M. S. Synthesis and characterization of magnetoelectric $\text{ba}_7\text{mn}_4\text{o}_{15}$. *Inorg. Chem.* **61**, 10015–10022 (2022).
- [20] Dey, U., Senn, M. S. & Bristowe, N. C. First-principles investigation of the magnetoelectric properties of $\text{ba}_7\text{mn}_4\text{o}_{15}$. *J. Phys.: Condens. Matter* **36**, 095701 (2023).
- [21] Rahmani, R. *et al.* Low-cost preparation of $\text{la}_4\text{co}_3\text{o}_9$ perovskite thin films with distinct absorbance ability and ferromagnetic behaviour. *Ceram. Int.* **48**, 26432–26439 (2022).
- [22] Hansteen, O. H., Fjellvåg, H. & Hauback, B. C. Crystal structure, thermal and magnetic properties of $\text{la}_4\text{co}_3\text{o}_9$. phase relations for $\text{la}_4\text{co}_3\text{o}_{10-\delta}$ ($0.00 \leq \delta \leq 1.00$) at 673 k. *J. Mater. Chem.* **8**, 2089–2093 (1998).
- [23] Ruddlesden, S. & Popper, P. The compound $\text{sr}_3\text{ti}_2\text{o}_7$ and its structure. *Acta Cryst.* **11**, 54–55 (1958).
- [24] Colville, A. & Geller, S. The crystal structure of brownmillerite, ca_2feal_5 . *Acta Cryst. B* **27**, 2311–2315 (1971).
- [25] Barrier, N. *et al.* Ferrite $\text{sr}_3\text{ndfe}_3\text{o}_9$: An original intergrowth between the brownmillerite and k_2nif_4 -type structures. *Chem. Mater.* **17**, 6619–6623 (2005).
- [26] Muñoz, A. *et al.* Crystallographic and magnetic structure of $\text{srcoo}_{2.5}$ brownmillerite: Neutron study coupled with band-structure calculations. *Phys. Rev. B* **78**, 054404 (2008).
- [27] Young, J. & Rondinelli, J. M. Crystal structure and electronic properties of bulk and thin film brownmillerite oxides. *Phys. Rev. B* **92**, 174111 (2015).
- [28] Tian, H., Bellaiche, L. & Yang, Y. Diversity of structural phases and resulting control of properties in brownmillerite oxides: A first-principles study. *Phys. Rev. B* **100**, 220103 (2019).

- [29] Arras, R., Paillard, C. & Bellaiche, L. Effect of an electric field on ferroelectric and piezoelectric properties of brownmillerite $\text{Ca}_2\text{Al}_2\text{O}_5$. *Phys. Rev. B* **107**, 144107 (2023).
- [30] Grenier, J.-C., Darriet, J., Pouchard, M. & Hagenmuller, P. Mise en évidence d'une nouvelle famille de phases de type perovskite lacunaire ordonnée de formule $\text{A}_3\text{M}_3\text{O}_8$ ($\text{A}=\text{Ca}, \text{Sr}$). *Mater. Res. Bull.* **11**, 1219–1225 (1976).
- [31] Luo, K. & Hayward, M. A. The synthesis and characterisation of $\text{LaCa}_2\text{Fe}_2\text{GaO}_8$. *J. of Solid State Chem.* **198**, 203–209 (2013).
- [32] Shin, Y. & Galli, G. Tunable ferroelectricity in oxygen-deficient perovskites with grenier structure. *npj Comput. Mater.* **9**, 218 (2023).
- [33] Zhang, J. *et al.* A correlated ferromagnetic polar metal by design. *Nature Materials* 1–8 (2024).
- [34] Fjellvåg, Ø. S., Øygarden, V., Sørby, M. H. & Sjåstad, A. O. Crystal structure of $\text{LaSr}_3\text{Fe}_3\text{O}_9$ and its phase relation with $\text{LaSr}_3\text{Fe}_3\text{O}_{10}$. *J. Solid State Chem.* **275**, 56–62 (2019).
- [35] Øygarden, V., Fjellvåg, H., Sørby, M. H. & Sjåstad, A. O. Crystal structure of $\text{LaSr}_3\text{Fe}_3\text{O}_8(\text{OH})_2 \cdot x\text{H}_2\text{O}$. *Inorg. Chem.* **55**, 7630–7636 (2016).
- [36] Jantsky, L., Okamoto, H., Demont, A. & Fjellvåg, H. Tuning of water and hydroxide content of intercalated ruddlesden-popper-type oxides in the $\text{PrSr}_3\text{Co}_{1.5}\text{Fe}_{1.5}\text{O}_{10-\delta}$ system. *Inorg. Chem.* **51**, 9181–9191 (2012).
- [37] Krüger, H., Stöber, S., Welberry, T., Withers, R. & Fitz Gerald, J. Stacking faults and superstructures in a layered brownmillerite. *Acta Crystallogr. B. Struct. Sci.* **67**, 476–485 (2011).
- [38] Tian, H. *et al.* Novel type of ferroelectricity in brownmillerite structures: A first-principles study. *Phys. Rev. Materials* **2**, 084402 (2018).
- [39] Parsons, T. G., D'Hondt, H., Hadermann, J. & Hayward, M. A. Synthesis and structural characterization of $\text{La}_{1-x}\text{A}_x\text{MnO}_{2.5}$ ($\text{A}=\text{Ba}, \text{Sr}, \text{Ca}$) phases: mapping the variants of the brownmillerite structure. *Chem. Mater.* **21**, 5527–5538 (2009).
- [40] Yamada, K. *et al.* Successive antiferromagnetic phase transitions in single-crystal La_2CoO_4 . *Phys. Rev. B* **39**, 2336 (1989).
- [41] Babkevich, P., Prabhakaran, D., Frost, C. & Boothroyd, A. Magnetic spectrum of the two-dimensional antiferromagnet La_2CoO_4 studied by inelastic neutron scattering. *Phys. Rev. B* **82**, 184425 (2010).
- [42] Scott, E. A. e. a. $\text{Bi}_2\text{CoO}_2\text{F}_4$ —a polar, ferrimagnetic aurivillius oxide-fluoride. *Chem. Mater.* **34**, 9775–9785 (2022).
- [43] Mulder, A. T., Benedek, N. A., Rondinelli, J. M. & Fennie, C. J. Turning ABo_3 antiferroelectrics into ferroelectrics: design rules for practical rotation-driven ferroelectricity in double perovskites and $\text{A}_3\text{B}_2\text{O}_7$ ruddlesden-popper compounds. *Adv. Funct. Mater.* **23**, 4810–4820 (2013).
- [44] Kang, K. T. *et al.* A room-temperature ferroelectric ferromagnet in a 1d tetrahedral chain network. *Adv. Mater.* **31**, 1808104 (2019).
- [45] Olafsen, A., Fjellvåg, H. & Hauback, B. C. Crystal structure and properties of $\text{Nd}_4\text{Co}_3\text{O}_{10+\delta}$ and $\text{Nd}_4\text{Ni}_3\text{O}_{10-\delta}$. *J. Solid State Chem.* **151**, 46–55 (2000).
- [46] McCabe, E. *et al.* Weak spin interactions in mott insulating $\text{La}_2\text{O}_2\text{Fe}_2\text{Ose}_2$. *Phys. Rev. B* **89**, 100402 (2014).
- [47] Porter, D. *et al.* Guiding antiferromagnetic transitions in Ca_2RuO_4 . *Sci. Rep* **12**, 10957 (2022).
- [48] Lu, N. *et al.* Electric-field control of tri-state phase transformation with a selective dual-ion switch. *Nature* **546**, 124–128 (2017).
- [49] Mou, X. *et al.* Analog memristive synapse based on topotactic phase transition for high-performance neuromorphic computing and neural network pruning. *Sci. Adv* **7**, eabh0648 (2021).
- [50] Forslund, R. P. *et al.* Exceptional electrocatalytic oxygen evolution via tunable charge transfer interactions in $\text{La}_{0.5}\text{Sr}_{1.5}\text{Ni}_{1-x}\text{Fe}_x\text{O}_{4\pm\delta}$ ruddlesden-popper oxides. *Nat. Commun.* **9**, 3150 (2018).
- [51] Liu, S., Sun, C., Chen, J., Xiao, J. & Luo, J.-L. A high-performance ruddlesden-popper perovskite for bifunctional oxygen electrocatalysis. *ACS Catal.* **10**, 13437–13444 (2020).
- [52] Blancon, J.-C., Even, J., Stoumpos, C. C., Kanatzidis, M. G. & Mohite, A. D. Semiconductor physics of organic-inorganic 2d halide perovskites. *Nat. Nanotechnol.* **15**, 969–985 (2020).
- [53] Tsai, H. *et al.* High-efficiency two-dimensional ruddlesden-popper perovskite solar cells. *Nature* **536**, 312–316 (2016).
- [54] Dashwood, C. *et al.* Strain control of a bandwidth-driven spin reorientation in CaRu_2O_7 . *Nat. Commun.* **14**, 6197 (2023).
- [55] Marković, I. *et al.* Electronically driven spin-reorientation transition of the correlated polar metal CaRu_2O_7 . *Proc. Natl. Acad. Sci.* **117**, 15524–15529 (2020).
- [56] Kresse, G. & Furthmüller, J. Efficiency of ab-initio total energy calculations for metals and semiconductors using a plane-wave basis set. *Comput. Mater. Sci.* **6**, 15–50 (1996).
- [57] Perdew, J. P. *et al.* Restoring the density-gradient expansion for exchange in solids and surfaces. *Phys. Rev. Lett.* **100**, 136406 (2008).
- [58] Blöchl, P. E. Projector augmented-wave method. *Phys. Rev. B* **50**, 17953–17979 (1994).
- [59] Dudarev, S. L., Botton, G. A., Savrasov, S. Y., Humphreys, C. J. & Sutton, A. P. Electron-energy-loss spectra and the structural stability of nickel oxide: An lsd+u study. *Phys. Rev. B* **57**, 1505–1509 (1998).
- [60] Pickett, W. E., Erwin, S. C. & Ethridge, E. C. Reformulation of the LDA + u method for a local-orbital basis. *Phys. Rev. B* **58**, 1201–1209 (1998).
- [61] Gebhardt, J. & Elsässer, C. Dft with corrections for an efficient and accurate description of strong electron correlations in nio. *J. Phys. Condens. Matter* **35**, 205901 (2023).
- [62] Uma, S. *et al.* Synthesis and characterization of sodium-iron antimonate $\text{Na}_2\text{FeSbO}_5$: One-dimensional antiferromagnetic chain compound with a spin-glass ground state. *Inorg. Chem.* **58**, 11333–11350 (2019).
- [63] Almoussawi, B. *et al.* Preparation, characterization and dft+u study of the polar Fe^{3+} -based phase $\text{Ba}_5\text{Fe}_2\text{ZnIn}_4\text{S}_{15}$ containing $s=5/2$ zigzag chains. *Dalton Trans.* **51**, 9522–9530 (2022).
- [64] Liechtenstein, A. I., Anisimov, V. I. & Zaanen, J. Density-functional theory and strong interactions: Orbital ordering in mott-hubbard insulators. *Phys. Rev. B* **52**, R5467–R5470 (1995).
- [65] Togo, A. & Tanaka, I. First principles phonon calculations in materials science. *Scr. Mater.* **108**, 1–5 (2015).

- [66] King-Smith, R. D. & Vanderbilt, D. Theory of polarization of crystalline solids. *Phys. Rev. B* **47**, 1651–1654 (1993).
- [67] Vanderbilt, D. & King-Smith, R. D. Electric polarization as a bulk quantity and its relation to surface charge. *Phys. Rev. B* **48**, 4442–4455 (1993).
- [68] H. T. Stokes, D. M. Hatch, and B. J. Campbell, ISOTROPY Software Suite, iso.byu.edu.
- [69] Momma, K. & Izumi, F. Vesta 3 for three-dimensional visualization of crystal, volumetric and morphology data. *J. Appl. Cryst.* **44**, 1272–1276 (2011).

ACKNOWLEDGMENTS

U.D. and N.C.B. acknowledge the Leverhulme Trust for a research project grant (Grant No. RPG-2020-206). This work made use of the facilities of the N8 Centre of Excellence in Computationally Intensive Research (N8 CIR) provided and funded by the N8 research partnership and EPSRC (Grant No. EP/T022167/1). The Centre is co-ordinated by the Universities of Durham, Manchester and York. This work also used the ARCHER2 UK National Supercomputing Service (<https://www.archer2.ac.uk>) and the Hamilton HPC Service of Durham University. We acknowledge useful discussions with Jorge Íñiguez and Mark S. Senn.

AUTHOR CONTRIBUTIONS

N.C.B. conceived the original project plan. E.E.M. highlighted previous studies on $A_4B_3O_9$ systems. U.D. performed all DFT simulations, supervised by N.C.B. U.D. performed all the symmetry analyses under the guidance of N.C.B. and E.E.M. U.D. wrote the first draft of the paper, and all authors contributed to re-drafting of the manuscript.

COMPETING INTERESTS

There are no competing interests associated with this paper.

MATERIALS & CORRESPONDENCE

Correspondence and requests for materials should be addressed to Nicholas C. Bristowe.

SUPPLEMENTARY INFORMATION

Section S1 presents the additional results for the $A_4B_3O_9$ (A : La, Pr, Nd, Y; B : Co, Ni) layered oxides, while in Section S2 we present additional details for the $LaA'_3Fe_3O_9$ (A' : Sr, Ca) systems.

S1. $A_4B_3O_9$ (A : La, Pr, Nd; B : Co, Ni) LAYERED OXIDES

A. STRUCTURAL DETAILS

TABLE S1. Fully optimized lattice parameters and magnetic moments of the different structural phases of the considered $A_4B_3O_9$ (A : La, Pr, Nd, Y; B : Co, Ni) compounds calculated with G-AFM magnetic ordering using $U_{\text{eff}} = 5.0$ eV and 5.15 eV for the $3d$ states of Co and Ni, respectively. ΔE denotes the relative energy of different structural variants. Available experimental values are given in the parentheses for comparison. Note that hydration can lead to an expansion of the lattice parameter along the long axis [35] and might explain the slight overestimation of the a -lattice parameter in Ref. [22].

Layered oxide	Phase	ΔE (meV/f.u.)	DFT-optimized lattice parameters				Magnetic moments (μ_B)	
			a (\AA)	b (\AA)	c (\AA)	V_{cell} (\AA^3)	μ_{tetra}	μ_{octa}
La ₄ Co ₃ O ₉	<i>Cmcm</i>	630.26	27.6366	5.6561	5.4374	849.95	2.545	2.660
	<i>Cmc2₁</i>	0.42	28.0116	5.6812	5.3970	858.87	2.664	2.650
	<i>Pmcn</i>	0.00	28.0122	5.6808	5.3978	858.95	2.664	2.650
			(28.4600 [†]) (27.5487 [‡])	(5.6467 [†]) (5.8568 [‡])	(5.4356 [†]) (5.6950 [‡])	(873.52 [†]) (918.87 [‡])	(2.6 [†])	(3.0 [†])
Pr ₄ Co ₃ O ₉	<i>Cmcm</i>	1087.92	27.3384	5.6392	5.3930	831.41	2.666	2.655
	<i>Cmc2₁</i>	0.11	27.7783	5.6749	5.3414	842.02	2.668	2.647
	<i>Pmcn</i>	0.00	27.7796	5.6749	5.3420	842.14	2.668	2.647
Nd ₄ Co ₃ O ₉	<i>Cmcm</i>	1266.50	27.9075	5.3850	5.2727	792.39	2.477	2.612
	<i>Cmc2₁</i>	0.00	27.7716	5.5427	5.4997	846.56	2.666	2.672
	<i>Pmcn</i>	3.20	27.7353	5.5943	5.4326	842.92	2.669	2.663
Y ₄ Co ₃ O ₉	<i>Cmcm</i>	2524.58	27.2707	5.2982	5.2050	752.04	2.488	2.630
	<i>Cmc2₁</i>	0.00	25.9609	5.3990	5.6600	793.33	2.684	2.694
	<i>Pmcn</i>	35.10	26.0835	5.3795	5.6971	799.40	2.684	2.695
La ₄ Ni ₃ O ₉	<i>Cmcm</i>	552.09	27.5656	5.5510	5.4521	834.26	1.550	1.650
	<i>Cmc2₁</i>	0.00	28.0082	5.5801	5.3886	842.18	1.683	1.640
	<i>Pmcn</i>	0.15	28.0105	5.5794	5.3886	842.14	1.683	1.640
Pr ₄ Ni ₃ O ₉	<i>Cmcm</i>	729.75	27.4044	5.5399	5.3886	818.10	1.542	1.646
	<i>Cmc2₁</i>	0.00	27.6193	5.6322	5.3250	828.35	1.690	1.636
	<i>Pmcn</i>	0.32	27.8083	5.5761	5.3244	825.60	1.690	1.636
Nd ₄ Ni ₃ O ₉	<i>Cmcm</i>	761.68	27.1764	5.5330	5.3644	806.62	1.547	1.646
	<i>Cmc2₁</i>	0.00	27.3093	5.6398	5.2944	815.44	1.702	1.639
	<i>Pmcn</i>	0.71	27.3126	5.6399	5.2933	815.38	1.702	1.639
Y ₄ Ni ₃ O ₉	<i>Cmcm</i>	1827.87	26.3662	5.4469	5.3291	765.34	1.587	1.662
	<i>Cmc2₁</i>	0.00	26.1242	5.3224	5.6156	780.82	1.703	1.670
	<i>Pmcn</i>	3.70	26.2506	5.2961	5.6520	785.78	1.708	1.674

[†] denotes the experimental values measured in Ref. [22].

[‡] denotes the experimental values measured in Ref. [21].

B. ELECTRONIC PROPERTIES

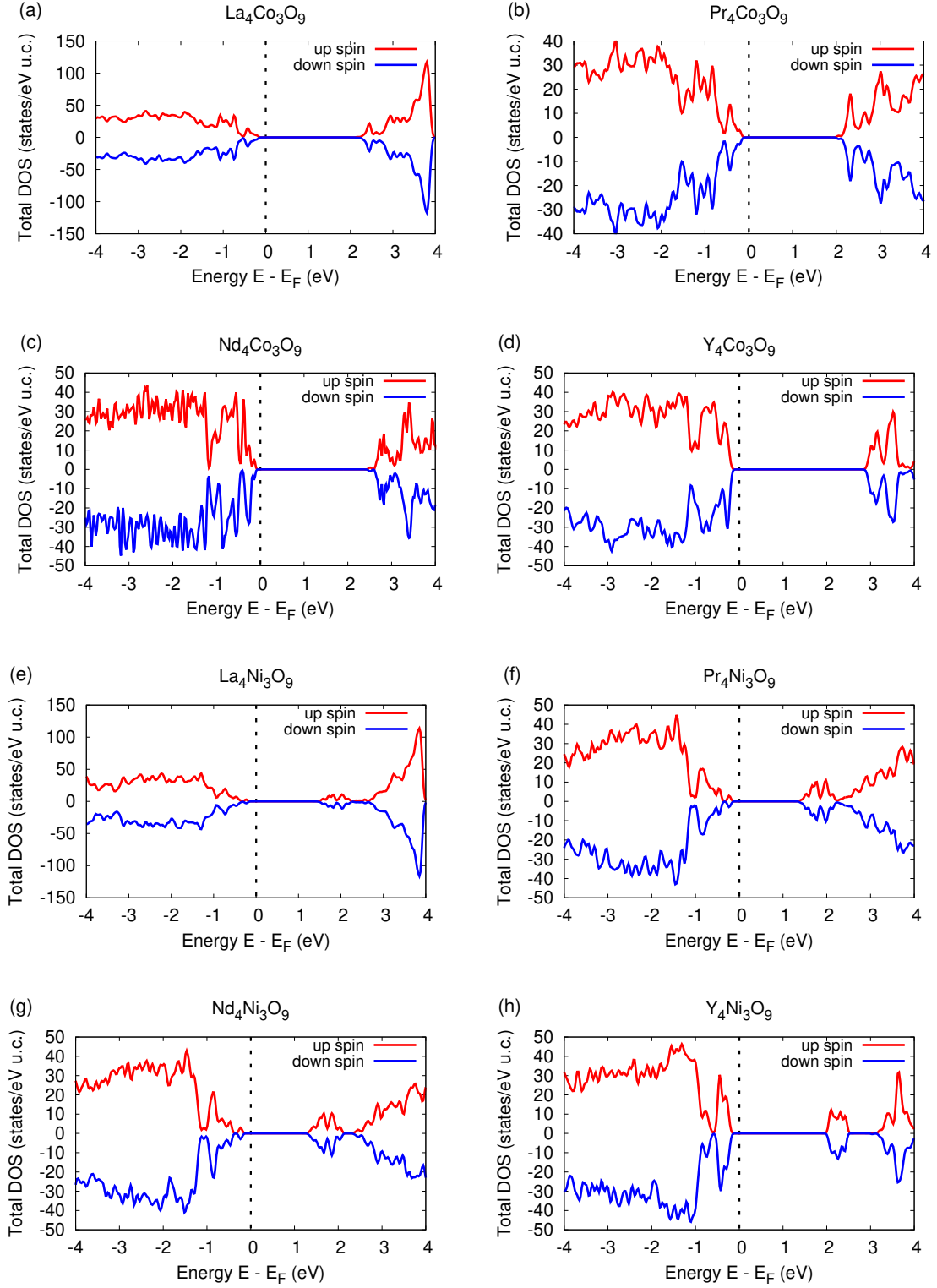


FIG. S1. Total density of states (DOS) calculated for the lowest energy phases of $A_4B_3O_9$ (A : La, Pr, Nd, Y; B : Co, Fe) compounds (see Table S1) showing the insulating nature of the considered layered oxides. G-AFM magnetic order is considered with $U_{\text{eff}} = 5.0$ eV and 5.15 eV for the 3d states of Co and Ni, respectively.

C. GROUND STATE MAGNETIC CONFIGURATIONS

Considering four initial spin arrangements of the B -site cations along the c -direction, namely the ferromagnetic (FM), A-type antiferromagnetic (A-AFM), C-type antiferromagnetic (C-AFM) and G-type antiferromagnetic (G-AFM), shown in Fig. S2, we calculate the ground state magnetic configuration for the lowest energy nuclear structure of the considered layered oxides given in Table S1. Furthermore, we identify C*- and G*-AFM spin configurations, shown in Fig. S2, which are very close in energy to the C- and G-AFM configurations, respectively (see Table S2). The very small energy difference can be attributed to the very weak coupling between the two triple-layered perovskite blocks within the unit cell (see Table S7). Note that C-AFM, C*-AFM, G-AFM and G*-AFM configurations have identical energies in the parent $I4/mmm$ phase of the oxidized $A_4B_3O_{10}$ compounds, but possess different energies in presence of oxygen vacancy-induced octahedral rotations and hence should be treated separately for the symmetry analyses of $A_4B_3O_9$ layered oxides. Similarly, it is possible to have F*- and A*-AFM configurations by changing the relative coupling between the perovskite blocks in the FM and A-AFM spin structures. However, since FM and A-AFM orderings are found to be higher in energy in the considered $A_4B_3O_{10}$ oxides (see Table S2), they are not discussed further.

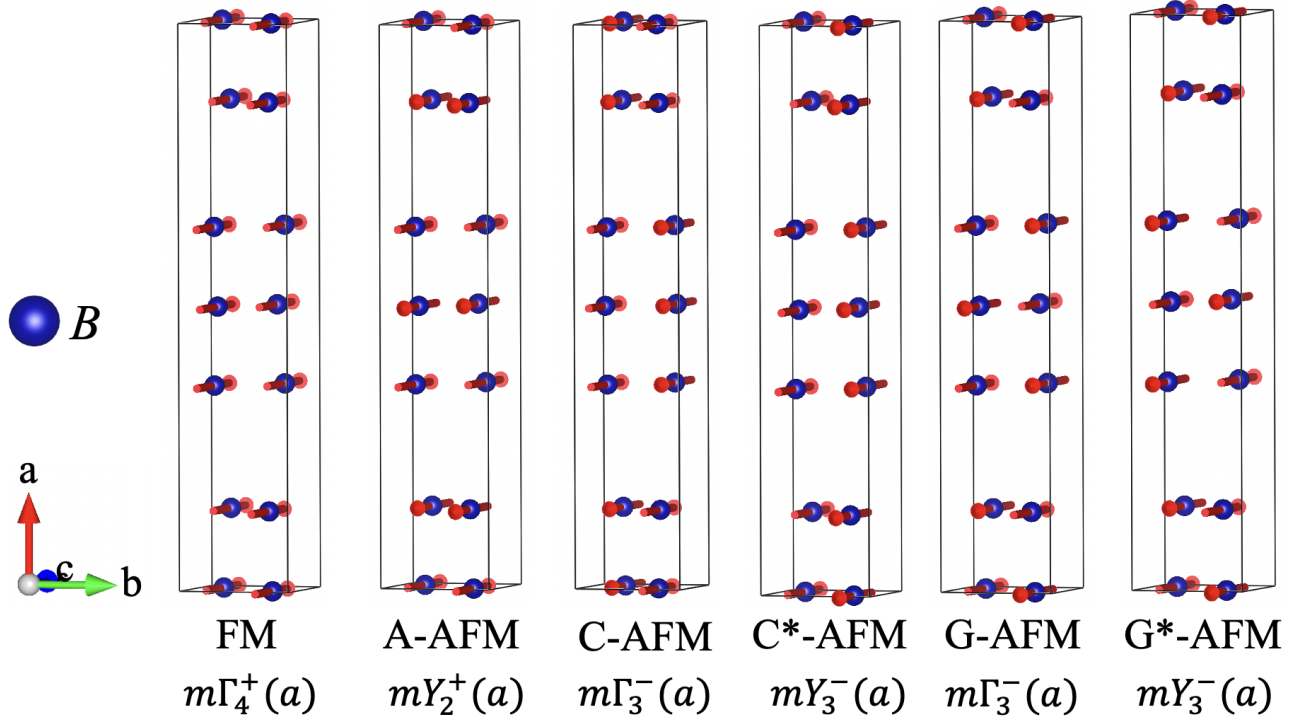


FIG. S2. Collinear spin configurations of the B -site cations considered for calculating the ground state magnetic structure of the $A_4B_3O_9$ layered oxides. The corresponding AFM irreps are also given. Spin magnetic moments are denoted by red arrows.

TABLE S2. Ground state (G.S.) magnetic configuration of the $A_4B_3O_9$ (A : La, Pr, Nd, Y; B : Co, Ni) layered oxides calculated for the lowest energy phases given in Table S1. $U_{\text{eff}} = 5.0$ eV and 5.15 eV are used for the $3d$ states of Co and Ni, respectively. Note that $\text{Nd}_4\text{Co}_3\text{O}_9$ and $\text{A}_4\text{Ni}_3\text{O}_9$ possess wFM in the polar $Cmc2_1$ structure required for the Γ -point switching scheme described in Fig. 1(b) of the main text. We have used the non-standard bca setting of the magnetic space group $Pn'm'a$ ($Pm'cn'$) to give the long axis along a for consistency with the rest of the paper. While the energy difference between G-(C-) and G*(C*-)AFM configurations is very small, we believe differences down to ~ 0.02 meV/f.u. are real since this appears to be the level of agreement between G-G* vs. C-C* AFM orderings (which are expected to be the same under the assumption of the 5 primary J exchange paths mentioned in section S1 G).

Layered oxide	Phase	Relative energy in meV/f.u.						G.S. magnetic space group	Polar mode	Magnetic modes present	wFM
		FM	A-AFM	C-AFM	C*-AFM	G-AFM	G*-AFM				
$\text{La}_4\text{Co}_3\text{O}_9$	$Pm\bar{c}n$	174.14	137.83	32.39	32.41	0.001	0.00	$Pm'cn'$	✘	$m\Gamma_4^+(a), mY_3^-(a)$	✓
$\text{Pr}_4\text{Co}_3\text{O}_9$	$Pm\bar{c}n$	176.80	138.71	34.68	34.63	0.06	0.00	$Pm'cn'$	✘	$m\Gamma_4^+(a), mY_3^-(a)$	✓
$\text{Nd}_4\text{Co}_3\text{O}_9$	$Cmc2_1$	172.90	136.88	31.57	31.71	0.00	0.13	$Cm'c2'_1$	✓	$m\Gamma_4^+(a), m\Gamma_3^-(a)$	✓
$\text{Y}_4\text{Co}_3\text{O}_9$	$Cmc2_1$	135.29	106.08	24.62	24.66	0.00	0.06	$Cm'c2'_1$	✓	$m\Gamma_4^+(a), m\Gamma_3^-(a)$	✓
$\text{La}_4\text{Ni}_3\text{O}_9$	$Cmc2_1$	267.72	286.44	0.00	0.28	21.54	21.78	$Cm'c2'_1$	✓	$m\Gamma_4^+(a), m\Gamma_3^-(a)$	✓
$\text{Pr}_4\text{Ni}_3\text{O}_9$	$Cmc2_1$	273.16	292.54	0.00	0.18	21.58	21.74	$Cm'c2'_1$	✓	$m\Gamma_4^+(a), m\Gamma_3^-(a)$	✓
$\text{Nd}_4\text{Ni}_3\text{O}_9$	$Cmc2_1$	259.64	278.81	0.00	0.15	20.55	20.69	$Cm'c2'_1$	✓	$m\Gamma_4^+(a), m\Gamma_3^-(a)$	✓
$\text{Y}_4\text{Ni}_3\text{O}_9$	$Cmc2_1$	119.63	144.31	0.00	0.06	38.89	38.97	$Cm'c2'_1$	✓	$m\Gamma_4^+(a), m\Gamma_3^-(a)$	✓

TABLE S3. Relative energies of the magnetic easy axis directions calculated for the lowest energy phases of $\text{Nd}_4\text{Co}_3\text{O}_9$ and $\text{Nd}_4\text{Ni}_3\text{O}_9$ as representatives of the Co- and Ni-series layered oxides, respectively. G-AFM spin ordering is considered for the noncollinear calculations including SOC. $U_{\text{eff}} = 5.0$ eV and 5.15 eV are used for the $3d$ states of Co and Ni, respectively.

Layered oxide	Phase	Relative energy in meV/f.u.		
		along a	along b	along c
$\text{Nd}_4\text{Co}_3\text{O}_9$	$Cmc2_1$	5.81	0.95	0.00
$\text{Nd}_4\text{Ni}_3\text{O}_9$	$Cmc2_1$	2.16	1.34	0.00

D. PHONON SPECTRA AND METASTABLE PHASES

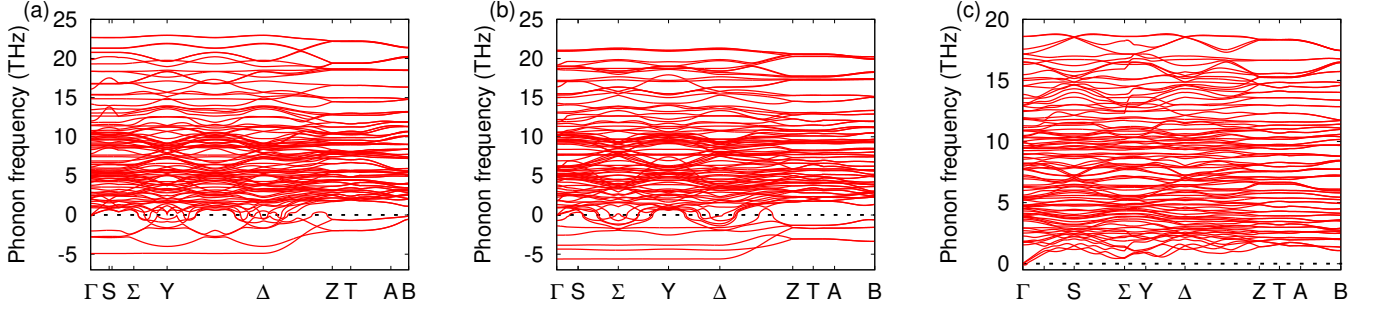


FIG. S3. Phonon spectra along the $\Gamma(0,0,0) - S(0,0.5,0) - \Sigma(0.25,0.25,0) - Y(0.5,0.5,0) - \Delta(0.75,0.25,0) - Z(0,0,0.5) - T(0.5,0.5,0.5) - A(0.25,0.25,0.5) - B(0.75,0.25,0.5)$ direction of the BZ (in the primitive basis) calculated with G-AFM magnetic order for the high symmetry $Cmcm$ phase of (a) $Nd_4Co_3O_9$ and (b) $Nd_4Ni_3O_9$ as representatives of the Co- and Ni-series $A_4B_3O_9$ layered oxides, respectively. $U_{\text{eff}} = 5.0$ eV and 5.15 eV are used for the 3d states of Co and Ni, respectively. As seen, all the Co- and Ni-series compounds have a strongly unstable flat phonon branch along the $\Gamma - S - \Sigma - Y - \Delta$ direction in the BZ associated with the tetrahedral chain ordering distortions. Panel (c) shows the phonon bands for the polar $Cm2_1$ phase of $Nd_4Co_3O_9$. Absence of imaginary phonon frequencies indicates the dynamical stability of this polar phase.

Phonon spectra in Fig. S3 show that the paraelectric $Cmcm$ phase of $A_4B_3O_9$ layered oxides is unstable against the tetrahedral chain ordering distortions. Therefore, in order to check the stability of the ground state polar $Cm2_1$ structure of $Nd_4B_3O_9$ (B : Co, Ni) (as a representative of the Ni-series compounds, see Table S1) with non-trivial ME effect, we condense in the phonon instabilities at the zone-center and zone-boundary points which result in a number of structural variants with different space group symmetries as shown in Fig. S4. Relative energies of the fully relaxed metastable structures are listed in Table S4. Note that we have limited our simulations to the 128 atom-superstructures to keep the computations tractable.

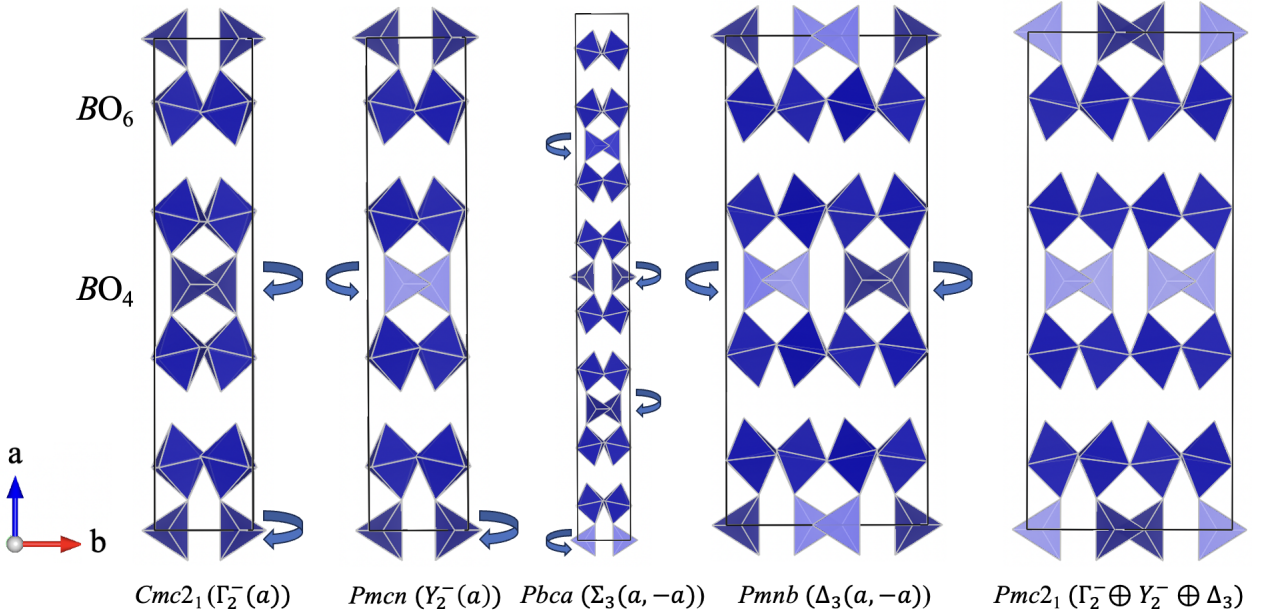


FIG. S4. Different structural phases of $A_4B_3O_9$ layered oxides arising from cooperative rotations of the tetrahedral units.

TABLE S4. Relative energies of the different metastable phases of $\text{Nd}_4\text{B}_3\text{O}_9$ (B : Co, Ni) arising from the relative ordering of the tetrahedral twisting patterns shown in Fig. S4. We have fully relaxed the structures with G-AFM spin order using $U_{\text{eff}} = 5.0$ eV and 5.15 eV for the $3d$ states of Co and Ni, respectively. Note that the polar $Cmc2_1$ phase is the ground state of $\text{Nd}_4\text{Co}_3\text{O}_9$ which allows for the Γ -point switching scheme described in Fig. 1(b) of the main text.

Phase	Irrep of primary order parameter(s)	Irreps of secondary order parameters	Relative energy in meV/f.u.	
			$\text{Nd}_4\text{Co}_3\text{O}_9$	$\text{Nd}_4\text{Ni}_3\text{O}_9$
$Cmc2_1$	$\Gamma_2^-(a)$	$\Gamma_1^+(a)$	0.00	8.55
$Pm\bar{c}n$	$Y_2^-(a)$	$\Gamma_1^+(a)$	3.20	9.28
$Pmab$	$\Sigma_3(0, a)$	$\Gamma_1^+(a)$ $Y_1^+(a)$	209.92	261.00
$Pbca$	$\Sigma_3(a, -a)$	$\Gamma_1^+(a)$ $Y_3^-(a)$	5.74	8.95
$Pmcb$	$\Delta_3(a, 0)$	$\Gamma_1^+(a)$ $Y_1^+(a)$	433.73	425.99
$Pmnb$	$\Delta_3(a, -a)$	$\Gamma_1^+(a)$ $Y_4^-(a)$	9.60	0.00
$Pmc2_1$	$\Gamma_2^-(a)$ $Y_2^-(a)$ $\Delta_3(0, a)$	$\Gamma_1^+(a)$ $\Delta_1(a, 0)$ $Y_1^+(a)$	9.84	4.41
$Cc2m$	$Z_2(a, 0)$	$\Gamma_1^+(a)$ $\Gamma_4^-(a)$	728.15	626.70

E. EFFECT OF U_{eff} ON THE GROUND STATE OF $\text{Nd}_4\text{Co}_3\text{O}_9$

In order to check the stability of the ground state magnetic configuration and crystal structure of $\text{Nd}_4\text{Co}_3\text{O}_9$, we consider two other extreme sets of U_{eff} values for the Co-3d states as described in Table S5 and find that polar $Cmc2_1$ phase with G-AFM spin ordering of the Co^{2+} ions is stable against different Hubbard U_{eff} parameters within reasonable range. Very small value of U_{eff} is, however, found to favor the antipolar structure.

TABLE S5. Stability of the polar $Cmc2_1$ phase of $\text{Nd}_4\text{Co}_3\text{O}_9$ as a function of the U_{eff} parameter. ΔE denotes the relative energies of the polar $Cmc2_1$ and antipolar $Pm\bar{c}n$ phases. Relative energies of the closely lying G-AFM and G*-AFM magnetic configurations are also given for the lowest energy phase in each case. As seen, polar $Cmc2_1$ phase with G-AFM spin ordering of the Co^{2+} ions is stable against different U_{eff} parameters within reasonable range. While the energy difference between G- and G*-AFM configurations is very small, we believe differences down to ~ 0.02 meV/f.u. are real (see Table S2 for details).

U_{eff} (eV)	Phase	ΔE (meV/f.u.)	Relative energy in meV/f.u.	
			G-AFM	G*-AFM
3.0	$Cmc2_1$	0.00	0.00	0.26
	$Pm\bar{c}n$	0.58		
5.0	$Cmc2_1$	0.00	0.00	0.13
	$Pm\bar{c}n$	3.20		
8.0	$Cmc2_1$	0.00	0.00	0.05
	$Pm\bar{c}n$	7.28		

F. EFFECT OF J ON THE WEAK FERROMAGNETIC MOMENT OF $\text{Nd}_4\text{Co}_3\text{O}_9$

TABLE S6. Effect of the Hund's parameter J on the net weak ferromagnetic (wFM) moment calculated with G-AFM magnetic configuration of Co^{2+} ions in the polar $Cmc2_1$ (+P state) phase of $\text{Nd}_4\text{Co}_3\text{O}_9$.

U (eV)	J (eV)	Net wFM moment ($\mu_B/\text{u.c.}$)
5.0	0.0	-0.18
5.5	0.5	-0.20
6.0	1.0	-0.24

G. MAGNETIC EXCHANGE INTERACTION PARAMETERS AND POSSIBILITY OF RT MAGNETISM IN $\text{Nd}_4\text{Co}_3\text{O}_9$

In order to investigate the possibility of RT magnetism in $\text{Nd}_4\text{Co}_3\text{O}_9$, we calculate the nearest neighbor (NN) magnetic exchange interaction parameters by mapping the DFT-calculated total energies of different magnetic structures onto the classical Heisenberg model:

$$H = - \sum_{\langle ij \rangle} J_{ij} \mathbf{S}_i \cdot \mathbf{S}_j \quad (1)$$

where J_{ij} denotes the magnetic exchange interaction between the NN i and j sites. $J > 0$ indicates FM spin interactions, while $J < 0$ denotes AFM interactions between the spins. J_{ij} runs from J_1 to J_5 as shown in Fig. S5. J_1 and J_2 denote the in-plane interactions between the NN octahedral and tetrahedral sites, respectively. On the other hand, J_3 is the NN out-of-plane spin interaction within the perovskite blocks. J_4 and J_5 are slightly inequivalent interlayer exchange interactions which gives rise to G-(C-) vs. G*-(C*)AFM configurations.

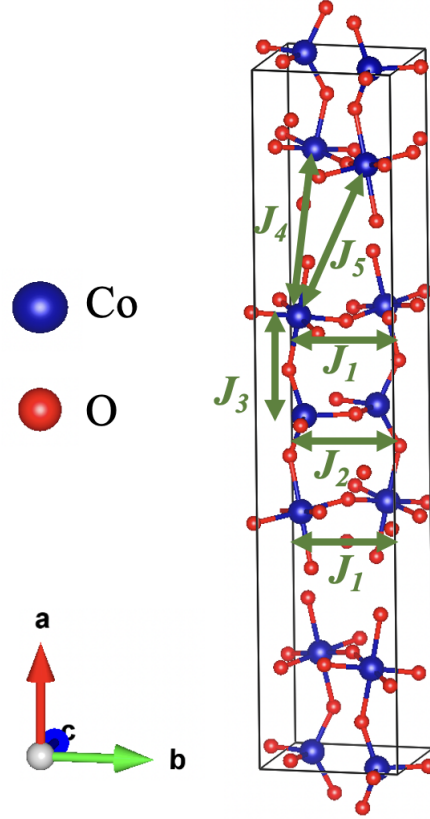


FIG. S5. Crystal structure of $\text{Nd}_4\text{Co}_3\text{O}_9$ showing different nearest neighbor spin exchange interaction parameters considered in our simulations.

Considering the two perovskite blocks to be identical, we calculate the NN spin exchange parameters for the ground state polar $Cmc2_1$ phase of $\text{Nd}_4\text{Co}_3\text{O}_9$ and compare the J 's with those computed for the experimentally observed antipolar $Pm\bar{c}n$ phase of $\text{La}_4\text{Co}_3\text{O}_9$. As seen from Table S7, the values of the corresponding J 's are almost identical. Therefore, in analogy with the experimental RT long-range G-AFM ordering of Co^{2+} ions in $\text{La}_4\text{Co}_3\text{O}_9$ [22], we predict RT G-AFM magnetic ordering in the ground state polar $Cmc2_1$ phase of $\text{Nd}_4\text{Co}_3\text{O}_9$. Hence, we put forward $\text{Nd}_4\text{Co}_3\text{O}_9$ as an ideal candidate to observe the electric field reversal of magnetization at RT with immense technological importance in the next generation memory devices.

TABLE S7. Nearest neighbor magnetic exchange interaction parameters calculated for $A_4\text{Co}_3\text{O}_9$ (A : La, Nd) using $U_{\text{eff}} = 5.0$ eV. As seen, the magnetic exchange parameters calculated for the polar $Cmc2_1$ phase of $\text{Nd}_4\text{Co}_3\text{O}_9$ are almost identical to those calculated for the experimentally observed $Pmcn$ phase of $\text{La}_4\text{Co}_3\text{O}_9$. Since a stronger J_4 gives rise to G-AFM ordering, rather than G^* -AFM ordering, this further supports the small energy differences between G- vs G^* -AFM configurations as being significant.

Layered oxide	Phase	J_1 (meV)	J_2 (meV)	J_3 (meV)	J_4 (meV)	J_5 (meV)
$\text{La}_4\text{Co}_3\text{O}_9$	$Pmcn$	-7.39	-1.50	-1.80	-0.44	-0.43
$\text{Nd}_4\text{Co}_3\text{O}_9$	$Cmc2_1$	-7.22	-2.01	-1.75	-0.51	-0.48

S2. $\text{LaA}'_3\text{Fe}_3\text{O}_9$ (A' : Sr, Ca) LAYERED OXIDES

A. CATION ORDERING MODELS

The high symmetry $Cmcm$ structure contains two inequivalent A sites (Wyckoff position $8g$), each with a multiplicity of two. Therefore, in order to model the $\text{LaA}'_3\text{Fe}_3\text{O}_9$ layered oxides, we have considered three different cation ordering models as described below.

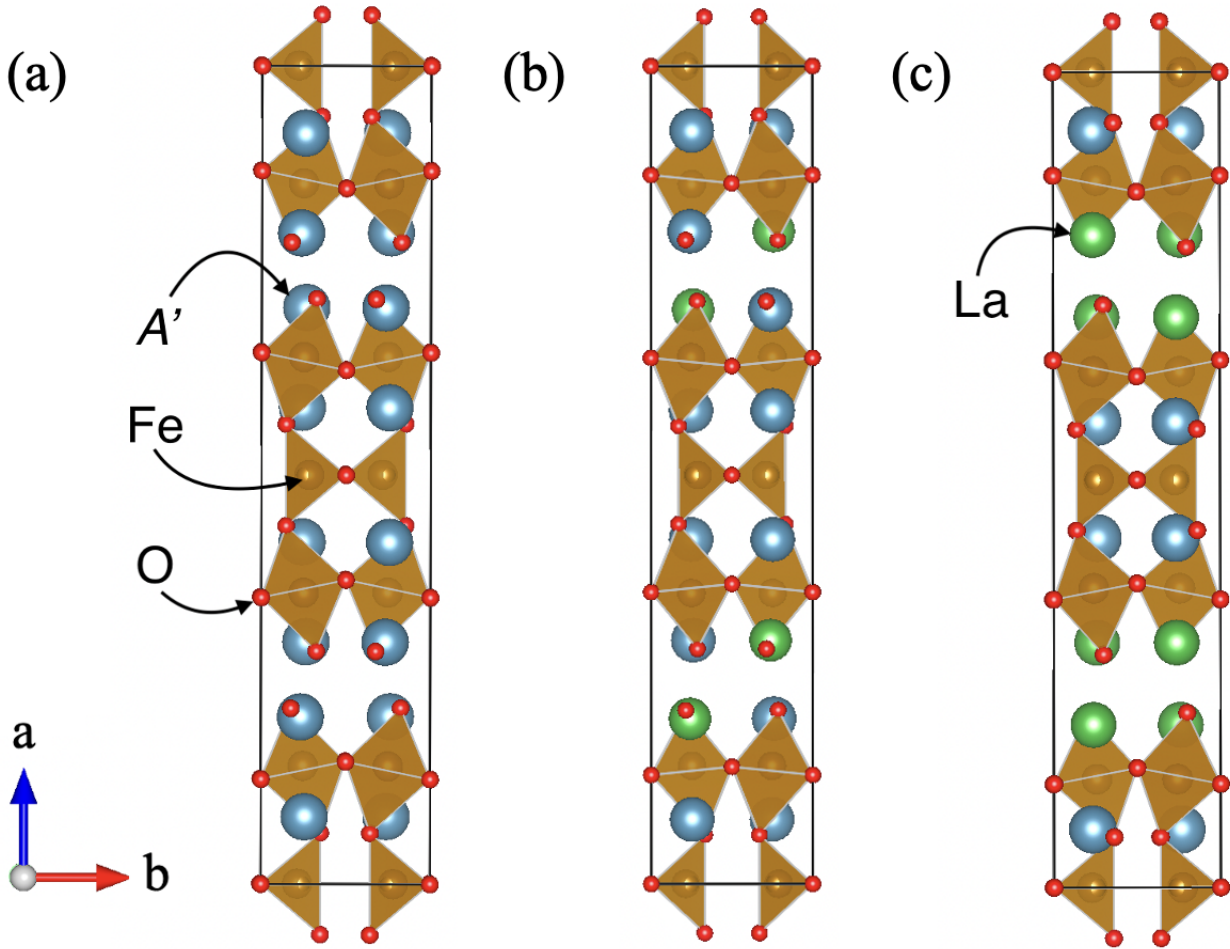


FIG. S6. Crystal structures within the (a) electron doped, (b) explicitly doped, and (c) hole doped cation ordering models considered to simulate the $\text{LaA}'_3\text{Fe}_3\text{O}_9$ ($A' = \text{Sr}, \text{Ca}$) layered oxides.

Electron doped model: In this model, we considered full occupancy of the A'^{2+} ions on the A sites. Four electrons are added to maintain the charge neutrality and 3+ valency of the Fe ions. The corresponding crystal structure is shown in Fig. S6(a).

Explicitly doped model: Four La atoms are added explicitly in the charge neutral four formula unit cell. The explicitly doped model breaks the symmetry of the original cell given in Table S8. The lowest energy crystal structure within this model is shown in Fig. S6(b).

Hole doped model: In the hole doped model, La^{3+} and A'^{2+} ions fully occupy the $A1$ and $A2$ sites. Our DFT calculations reveal that La prefers to occupy the A sites in the rocksalt layers as shown in Fig. S6(c). Similar to the electron doped model, four holes are added to maintain the charge neutrality and 3+ valency of the Fe ions.

B. STRUCTURAL DETAILS

TABLE S8. Fully optimized lattice parameters and magnetic moments of the different structural phases of the $\text{La}A'_3\text{Fe}_3\text{O}_9$ (A' : Sr, Ca) oxides calculated with ground state G-AFM magnetic ordering using $U_{\text{eff}} = 4.0$ eV for the $3d$ states of Fe. Available experimental values are given in the parentheses for comparison. Here, ΔE denotes the relative energy of different structural variants. The zero of energy corresponds to the polar $Cmcm$ structure. Note that the explicitly doped model breaks the symmetry of the original cell. The reduced symmetry space groups are given in the parentheses. As seen, the G.S. crystal structures of $\text{La}A'_3\text{Fe}_3\text{O}_9$ (A' : Sr, Ca) compounds are very sensitive to the cation ordering model considered.

Layered oxide	Cation ordering model	Phase	ΔE (meV/f.u.)	DFT-optimized lattice parameters				Magnetic moments (μ_B)	
				a (\AA)	b (\AA)	c (\AA)	V_{cell} (\AA^3)	μ_{tetra}	μ_{octa}
$\text{LaSr}_3\text{Fe}_3\text{O}_9$	Electron doped	$Cmcm$	437.77	28.7242	5.6731	5.6043	913.25	3.915	4.078
				(28.7559 [†])	(5.5279 [†])	(5.4582 [†])	(867.64 [†])	(3.58 [†])	(3.99 [†])
		$Cmc2_1$	0.00	29.2117	5.6347	5.5304	910.30	3.997	4.064
		$Pmcn$	-0.003	29.2126	5.6346	5.5306	910.34	3.997	4.064
	Explicitly doped	$Cmcm$ ($Pbnm$)	277.62	27.5944	5.6165	5.5314	857.27	3.888	4.094
		$Cmc2_1$ ($Pbn2_1$)	0.00	28.0063	5.5958	5.4822	859.17	3.983	4.085
		$Pmcn$ ($P2_12_12_1$)	-2.95	27.9938	5.5943	5.4885	859.54	3.983	4.086
	Hole doped	$Cmcm$	97.75	27.0699	5.5038	5.4232	807.99	3.859	4.085
		$Cmc2_1$	0.00	27.4933	5.4816	5.3903	812.36	3.961	4.076
$Pmcn$		0.08	27.4959	5.4811	5.3904	812.36	3.961	4.076	
$\text{LaCa}_3\text{Fe}_3\text{O}_9$	Electron doped	$Cmcm$	745.56	27.0879	5.6116	5.5485	843.41	3.933	4.093
		$Cmc2_1$	0.00	27.0320	5.5743	5.5447	835.49	4.007	4.090
		$Pmcn$	9.09	27.0918	5.5727	5.5461	837.31	4.007	4.090
	Explicitly doped	$Cmcm$ ($Pbnm$)	617.22	26.6787	5.5453	5.4670	808.80	3.913	4.095
		$Cmc2_1$ ($Pbn2_1$)	0.00	26.7691	5.5545	5.4089	804.25	4.010	4.089
		$Pmcn$ ($P2_12_12_1$)	-0.88	26.7656	5.5554	5.4084	804.19	4.010	4.088
	Hole doped	$Cmcm$	524.41	26.6036	5.4483	5.3688	778.18	3.888	4.079
		$Cmc2_1$	0.00	26.7898	5.4570	5.3183	777.49	4.006	4.066
		$Pmcn$	0.05	26.7909	5.45686	5.3184	777.51	4.006	4.066

[†] denotes the experimental values measured in Ref. [34].

C. ELECTRONIC PROPERTIES

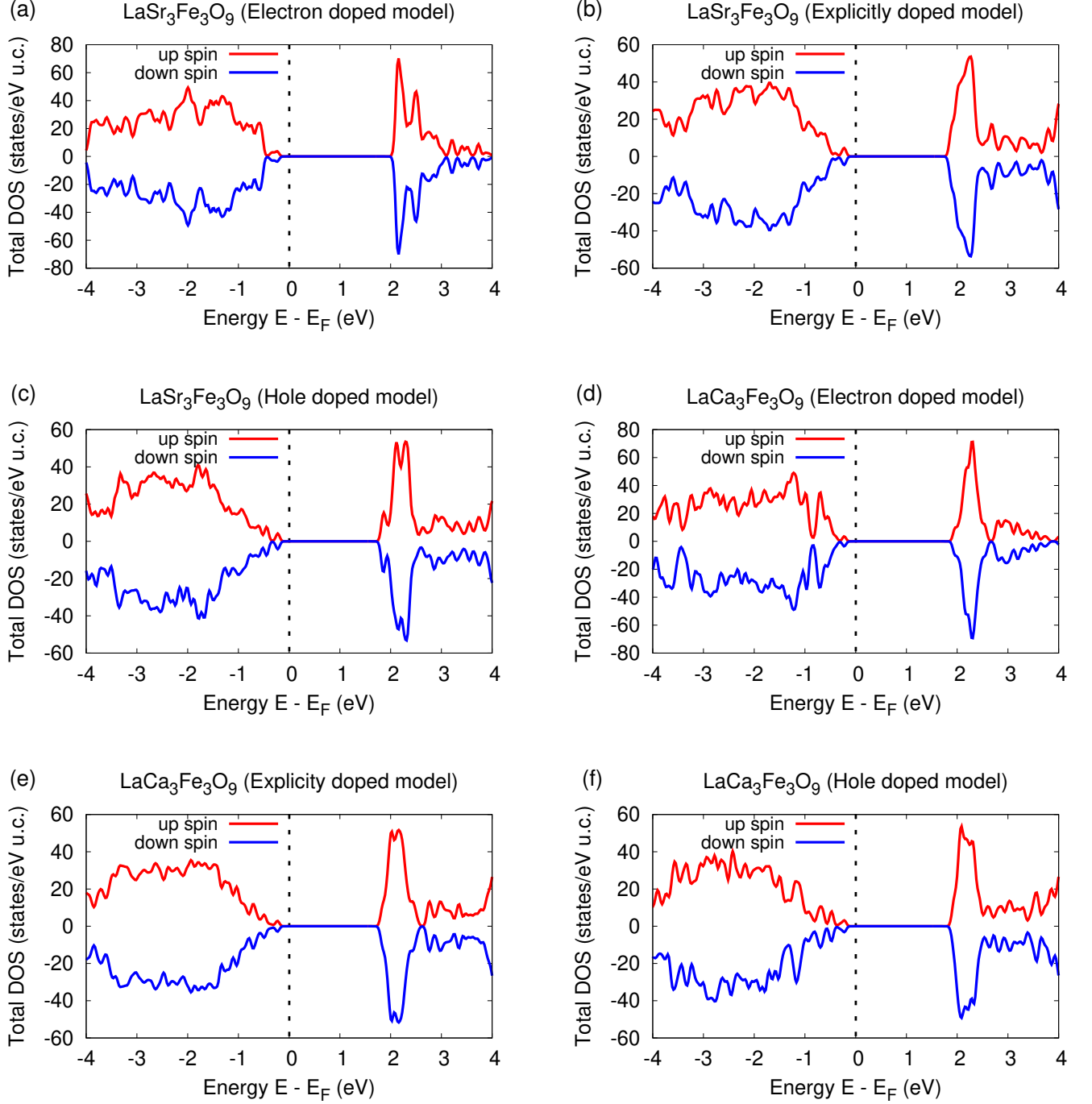


FIG. S7. Total density of states (DOS) calculated for the lowest energy phases of $\text{LaA}'_3\text{Fe}_3\text{O}_9$ (A' : Sr, Ca) compounds within different cation ordering models (see Table S8) showing the insulating nature of the considered layered oxides. G-AFM magnetic order is considered with $U_{\text{eff}} = 4.0$ eV for the $3d$ states of Fe.

D. GROUND STATE MAGNETIC CONFIGURATIONS

TABLE S9. Ground state (G.S.) magnetic configuration of the $\text{La}A'_4\text{Fe}_3\text{O}_9$ (A' : Sr, Ca) layered oxides calculated for the lowest energy phases given in Table S8. We use $U_{\text{eff}} = 4.0$ eV for the $3d$ states of Fe. Note that the explicitly doped model breaks the symmetry of the original cell. The reduced symmetry space groups are given in the parentheses. As seen, the G.S. magnetic structures of $\text{La}A'_4\text{Fe}_3\text{O}_9$ (A' : Sr, Ca) are very sensitive to the cation ordering model considered.

Layered oxide	Model	Phase	Relative energy in meV/f.u.						G.S. symmetry	Polar mode	Magnetic modes	wFM
			FM	A-AFM	C-AFM	C*-AFM	G-AFM	G*-AFM				
$\text{LaSr}_3\text{Fe}_3\text{O}_9$	Electron doped	$Pm\bar{c}n$	606.24	519.45	50.59	50.62	0.03	0.00	$Pm'\bar{c}n'$	✖	$m\Gamma_4^+(a)$ $mY_3^-(a)$	✓
	Explicitly doped	$Pm\bar{c}n$ ($P2_12_12_1$)	735.62	567.99	118.78	118.66	0.00	0.09	$Pm'\bar{c}n$ ($P2_12_1'2_1'$)	✖	$m\Gamma_3^-(a)$ $mY_4^+(a)$	✖
	Hole doped	$Cm\bar{c}2_1$	898.54	646.10	190.27	189.70	0.00	0.50	$Cm'\bar{c}2_1'$	✓	$m\Gamma_4^+(a)$ $m\Gamma_3^-(a)$	✓
$\text{LaCa}_3\text{Fe}_3\text{O}_9$	Electron doped	$Cm\bar{c}2_1$	571.17	448.58	91.99	92.06	0.50	0.00	$P_C\bar{b}c2_1$	✓	$mY_4^+(a)$ $mY_3^-(a)$	✖
	Explicitly doped	$Pm\bar{c}n$ ($P2_12_12_1$)	753.18	542.00	168.29	168.01	0.00	0.24	$Pm'\bar{c}n$ ($P2_12_1'2_1'$)	✖	$m\Gamma_3^-(a)$ $mY_4^+(a)$	✖
	Hole doped	$Cm\bar{c}2_1$	918.49	609.81	255.93	255.25	0.00	0.60	$Cm'\bar{c}2_1'$	✓	$m\Gamma_4^+(a)$ $m\Gamma_3^-(a)$	✓

TABLE S10. Relative energies of the magnetic easy axis directions calculated for the lowest energy phases of $\text{La}A'_3\text{Fe}_3\text{O}_9$ (A' : Sr, Ca) within the electron doped cation model. Ground state G-AFM spin ordering is considered for the noncollinear calculations including SOC. $U_{\text{eff}} = 4.0$ eV is used for the $3d$ states of Fe.

Layered oxide	Phase	Relative energy in meV/f.u.		
		along a	along b	along c
$\text{LaSr}_3\text{Fe}_3\text{O}_9$	$Pm\bar{c}n$	0.42	0.04	0.00
$\text{LaCa}_4\text{Fe}_3\text{O}_9$	$Cm\bar{c}2_1$	0.32	0.02	0.00

E. PHONON SPECTRA AND METASTABLE PHASES

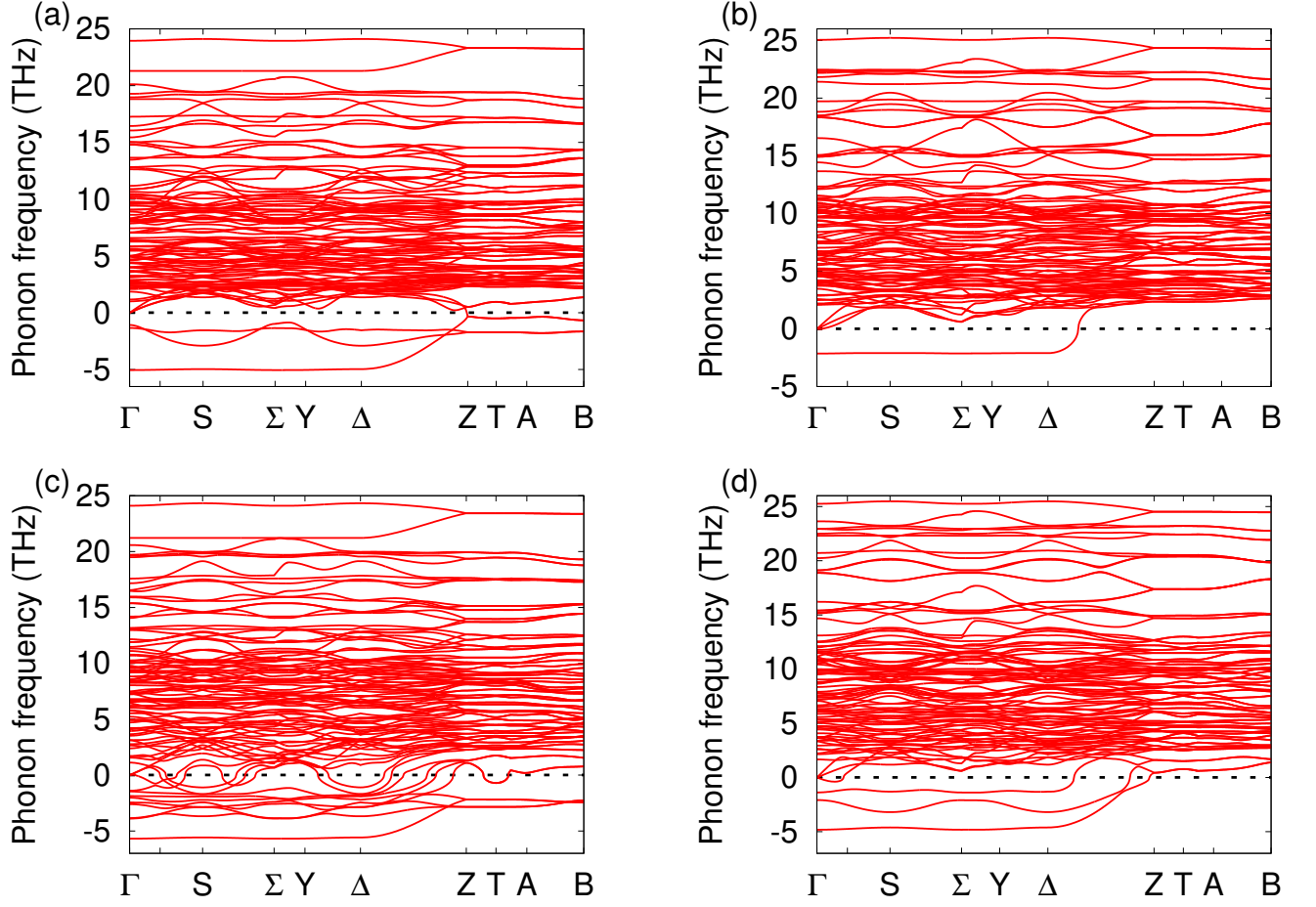


FIG. S8. (a)–(b) Phonon dispersion curves along the $\Gamma(0, 0, 0) - S(0, 0.5, 0) - \Sigma(0.25, 0.25, 0) - Y(0.5, 0.5, 0) - \Delta(0.75, 0.25, 0) - Z(0, 0, 0.5) - T(0.5, 0.5, 0.5) - A(0.25, 0.25, 0.5) - B(0.75, 0.25, 0.5)$ direction of the BZ (in the primitive basis) calculated with G-AFM magnetic order for the high symmetry $Cmcm$ phase of $\text{LaSr}_3\text{Fe}_3\text{O}_9$ in the electron doped (left) and hole doped (right) models. (c)–(d) Corresponding phonon bands of $\text{LaCa}_3\text{Fe}_3\text{O}_9$ in the electron doped (left) and hole doped (right) models. $U_{\text{eff}} = 4.0$ eV is used for the $3d$ states of Fe. Both the models show qualitatively similar features in the phonon spectra with a strongly unstable flat phonon branch along the $\Gamma - S - \Sigma - Y - \Delta$ direction in the BZ associated with the tetrahedral chain ordering distortions. The phonon spectra within explicitly doped model are not shown as the symmetry of the simulated unit cell differs from the $Cmcm$ symmetry of the original parent cell.

TABLE S11. Relative energies of the different metastable phases of $\text{La}A'_3\text{Fe}_3\text{O}_9$ (A' : Sr, Ca) within the electron doped model arising from the relative ordering of the tetrahedral twisting patterns shown in Fig. S4. We fully relaxed the structures with G-AFM spin order using $U_{\text{eff}} = 4.0$ eV for the $3d$ orbitals of Fe. Note that the polar $Cmc2_1$ phase is the ground state of $\text{LaCa}_3\text{Fe}_3\text{O}_9$ which allows for the Γ -point switching scheme described in Fig. 1(b) of the main text.

Phase	Irrep of primary order parameter	Irreps of secondary order order parameters	Relative energy in meV/f.u.	
			$\text{LaSr}_3\text{Fe}_3\text{O}_9$	$\text{LaCa}_4\text{Fe}_3\text{O}_9$
$Cmc2_1$	$\Gamma_2^-(a)$	$\Gamma_1^+(a)$	3.52	0.00
$Pmcn$	$Y_2^-(a)$	$\Gamma_1^+(a)$	3.51	9.09
$Pmab$	$\Sigma_3(0, a)$	$\Gamma_1^+(a)$ $Y_1^+(a)$	227.60	177.26
$Pbca$	$\Sigma_3(a, -a)$	$\Gamma_1^+(a)$ $Y_3^-(a)$	8.22	19.23
$Pmcb$	$\Delta_3(a, 0)$	$\Gamma_1^+(a)$ $Y_1^+(a)$	226.22	387.03
$Pmnb$	$\Delta_3(a, -a)$	$\Gamma_1^+(a)$ $Y_4^-(a)$	0.00	93.95
$Cc2m$	$Z_2(a, 0)$	$\Gamma_1^+(a)$ $\Gamma_4^-(a)$	414.31	614.35